

GW230814: investigation of a loud gravitational-wave signal observed with a single detector

THE LIGO SCIENTIFIC COLLABORATION, THE VIRGO COLLABORATION, THE KAGRA COLLABORATION, AND OTHERS

ABSTRACT

GW230814, detected by the LIGO Livingston observatory with a signal-to-noise ratio of 42.4 represents the loudest gravitational-wave signal in the GWTC-4.0 catalog. Its source is consistent with a binary black hole coalescence with component masses $m_1 = 33.7_{-2.2}^{+2.9} M_\odot$, $m_2 = 28.2_{-3.1}^{+2.2} M_\odot$, and a small effective inspiral spin $\chi_{\text{eff}} = -0.01_{-0.07}^{+0.06}$. The high signal-to-noise has enabled the first confident detection of an $\ell = |m| = 4$ mode in the inspiral phase, as well as detailed tests of waveform consistency with general relativity. While most of these tests show agreement with theoretical predictions, there are suggestions of minor deviations in the ringdown phase. Simulations that incorporate general relativity and realistic detector noise reproduce similar deviations, suggesting they do not constitute evidence for a breakdown of general relativity. The observation of GW230814 demonstrates that the unprecedented sensitivity of the detectors enables highly significant detections with a single observatory. However, without corroborating data from a multi-detector network, the ability to draw rigorous conclusions about fundamental physics remains severely limited.

1. INTRODUCTION

The gravitational wave (GW) signal GW230814.230901, henceforth referred to as GW230814, was observed by the LIGO Livingston observatory (LLO) at 2023-08-14 23:09:01.805 UTC. At the time of the observation, only LLO was taking data, with the LIGO Hanford, Virgo and KAGRA detectors offline. Despite this, the signal, with an inferred optimal signal-to-noise ratio (SNR) of $42.0_{-1.7}^{+1.6}$, is louder than any compact binary coalescence (CBC) published by the LIGO–Virgo–KAGRA collaboration (LVK) in the fourth Gravitational-Wave Transient Catalog (GWTC-4.0) (Abac et al. 2025a) or in non-LVK catalogs (Nitz et al. 2023; Wadekar et al. 2023). The Livingston data, shown in Fig. 1, clearly shows the presence of a loud binary black hole (BBH) coalescence signal. Despite being a single-detector event, the signal is the loudest CBC detected by the LVK in GWTC-4.0, and is of particular interest for its ability to constrain the properties of the source and the signal. In this work we expand upon the analysis presented in Abac et al. (2025b).

The signal was detected in low latency by the GstLAL pipeline (Sakon et al. 2024; Ewing et al. 2024; Tsukada et al. 2023) with an inverse false alarm rate (IFAR) greater than 10^5 years, and later confirmed by offline analysis of the data by both the GstLAL and PyCBC pipelines (Davies et al. 2020; Chandra et al. 2021; Davis et al. 2022; Kumar & Dent 2024). It was reported in GRACEDB as S230814ah (LVK Collaboration 2023).

The inferred intrinsic astrophysical parameters are similar to those observed for a number of other events (Abac et al. 2025b), including the first-ever GW detection GW150914 (Abbott et al. 2016). We find good consistency between results obtained with different waveform models, as expected for this part of parameter space which is well covered by numerical and theoretical models. The high SNR of the signal enables us to perform a range of consistency

tests between the data and theoretical expectations. We performed many of the standard suite of tests described in Abac et al. (2025c,d,e), finding that while most are consistent with the expectation of general relativity (GR) as described by the waveform models, there is an apparent deviation in the post-merger portion of the signal that we investigate further here. Our follow-up investigations suggest that these deviations are likely due to either systematic errors in waveform models or detector noise effects.

This paper is structured as follows. In Section 2, we present the detection of GW230814 and the measurement of its source properties. In Section 3 we present results of tests of GR that have been performed on the event, finding that some find an apparent deviation from GR in the post-merger portion of the signal. In Section 4 we detail further investigations to understand these results, focusing on data quality and waveform systematics. Our conclusions are discussed in Section 5.

GW observatory data, posterior samples and search information about GW230814 is available from The Gravitational Wave Open Science Centre (Abac et al. 2025f), and additional data used in the preparation of the paper is available at Abac et al. (2025g).

2. DETECTION AND PARAMETER ESTIMATES

2.1. Detector status and detection

At the time of the signal, the LLO was observing at a binary neutron star inspiral range (Finn & Chernoff 1993) of approximately 155 Mpc, consistent with its typical sensitivity during the observing run (Capote et al. 2025). The LIGO Hanford (Aasi et al. 2015), Virgo (Acernese et al. 2015), and KAGRA (Abbott et al. 2023a) detectors were not locked at the time of the event. Following standard GW detection-vetting procedures (Soni et al. 2025), no data-quality issues were reported at the time of the event in the LLO data. Fur-

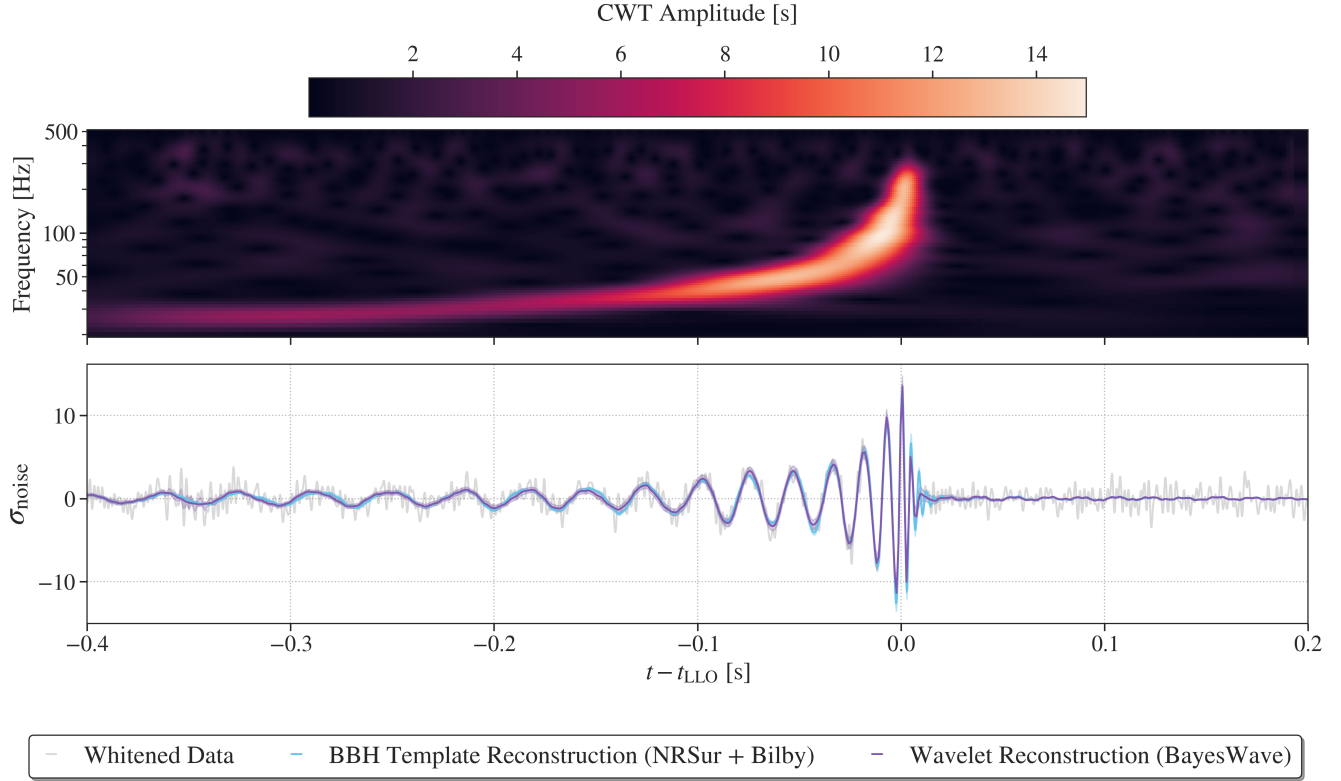


Figure 1. Time-frequency representation (top) and whitened time-domain strain with Bayesian reconstructions (bottom) from LIGO Livingston observations of GW230814. Time is measured relative to GPS time $t_{\text{LLO}} = 1376089759.805280$ s. The top panel shows the time-frequency representation of the whitened strain data, obtained using a continuous wavelet transform (CWT) with a Morlet–Gabor wavelet. The color scale represents the amplitude of the CWT coefficients, in units of seconds. The bottom panel displays the whitened strain data (gray) alongside 90% credible intervals from waveform reconstructions using the NRSUR7DQ4 (NRSur) model (blue) and the wavelet-based BayesWave algorithm (purple). The data are high-pass filtered at 20 Hz and downsampled to 1024 Hz in both panels.

ther details about the state of the detectors during O4a are provided in [Abac et al. \(2025a\)](#).

The signal was identified by the low-latency GstLAL pipeline ([Messick et al. 2017](#); [Sachdev et al. 2019](#); [Hanna et al. 2020](#); [Cannon et al. 2020](#); [Sakon et al. 2024](#); [Ewing et al. 2024](#); [Tsukada et al. 2023](#)) as a statistically significant deviation from the noise background, with a matched-filter SNR of 42.4 and an IFAR exceeding 10^5 years. The PyCBC Live ([Usman et al. 2016](#); [Nitz et al. 2017](#); [Dal Canton et al. 2021](#)) and MBTA ([Adams et al. 2016](#); [Aubin et al. 2021](#); [Alléné et al. 2025](#)) low latency pipelines are capable of detecting signals in single detector data, but did not identify the event, as they are configured to report only on single-detector signals with potential electromagnetic counterparts, typically those with template durations longer than 7 s. The event was not detected by search algorithms like coherent WaveBurst ([Klimenko et al. 2016](#)) and SPIIR ([Chu et al. 2022](#)), which rely on coherence of signals in multiple detectors.

In general, the IFARs assigned to single-detector candidates carry greater uncertainty than those associated with multi-detector events because the background distribution is derived solely from triggers in one detector and cannot be combined with backgrounds from other instruments ([Sachdev et al. 2019](#); [Nitz et al. 2020](#); [Davies & Harry](#)

	GstLAL	PyCBC
Offline SNR	42.3	43.0
Online inverse FAR (yr)	$> 10^5$	-
Offline inverse FAR (yr)	$> 10^5$	> 1000

Table 1. Significance and matched-filter SNR of GW230814 in two different search pipelines discussed in the text.

[2022](#); [Alléné et al. 2025](#)). The uncertainty is most important for marginally significant triggers near the tails of the background distribution, where statistical support is weak and constraints inherently poor. In contrast, triggers that fall within the bulk of the background and are consistent with noise, or those that are clearly separated from the noise distribution and consistent with a signal (like this event), can still be reliably identified ([Abbott et al. 2020](#)).

Subsequent offline analysis using refined data-quality information and improved background estimation reaffirmed GstLAL’s original significance estimate, also resulting in an IFAR greater than 10^5 years. Furthermore, as summarised in Table 1, the offline PyCBC search ([Davies et al. 2020](#); [Chandra et al. 2021](#); [Davis et al. 2022](#); [Kumar & Dent 2024](#)) also

Parameter	Value
$m_1 (M_\odot)$	$33.7^{+2.9}_{-2.2}$
$m_2 (M_\odot)$	$28.2^{+2.2}_{-3.1}$
Chirp Mass $\mathcal{M} (M_\odot)$	$26.8^{+0.9}_{-1.0}$
Total Mass $M (M_\odot)$	$61.9^{+2.0}_{-2.0}$
Mass ratio $q = m_2/m_1$	$0.84^{+0.12}_{-0.14}$
χ_{eff}	$-0.01^{+0.06}_{-0.07}$
Final mass (detector frame) $M_f^{\text{det}} (M_\odot)$	$62.7^{+1.5}_{-1.4}$
Final spin χ_f	$0.68^{+0.02}_{-0.02}$
$\cos(\theta_{JN})$	$0.0^{+0.7}_{-0.7}$
D_L (Mpc)	289^{+183}_{-130}
Redshift z	$0.06^{+0.04}_{-0.03}$
Optimal SNR	$42.0^{+1.6}_{-1.7}$
Matched filter SNR	$42.13^{+0.07}_{-0.11}$

Table 2. Selected parameters of the source averaged over the different waveform models used. The value quoted is the median and the uncertainty indicates the 90% credible interval.

identified the event, assigning it an IFAR exceeding 1000 years. The reported statistical significances reflect the maximum IFAR permitted by each pipeline for single-detector events, as defined by their configuration choices. We therefore conclude with high confidence that this event is not of terrestrial origin.

2.2. Source properties

Parameter estimation (PE) was performed using the BILBY package (Ashton et al. 2019; Romero-Shaw et al. 2020), following an analysis setup consistent with GWTC-4.0 (Abac et al. 2025h) and four waveform models: SEOBNRv5PHM (SEOBNR) (Pompili et al. 2023; Khalil et al. 2023; van de Meent et al. 2023; Ramos-Buades et al. 2023), IMRPHENOMXPHM_SPINTAYLOR (XPHM) (Pratten et al. 2021; Colleoni et al. 2025), IMRPHENOMXO4A (XO4a) (Hamilton et al. 2021; Thompson et al. 2024), and NRSUR7DQ4 (NRSur) (Varma et al. 2019). The analysis used 8 s of data around the trigger time, considering the frequency range between 24 Hz and 448 Hz. This choice ensured that $\ell = |m| = 3$ subdominant modes were fully included in the analysis. The inferred signal, marginalized over the uncertainty in the source parameters, is shown in Figure 1, which indicates the 90% credible region for the NRSur waveform. We also show a wavelet reconstruction of the signal with the BayesWave algorithm (Cornish & Littenberg 2015; Bécsy et al. 2017; Cornish et al. 2021, 2024), which we find is consistent with that from the NRSur model. However, we observe that the BayesWave reconstruction has a quicker amplitude decay than the NRSur reconstruction.

Table 2 shows the selected source parameters. Unless otherwise noted, we report the parameter estimates averaged equally across waveform models, and quote the median and 90% credible interval of the posterior probability distribu-

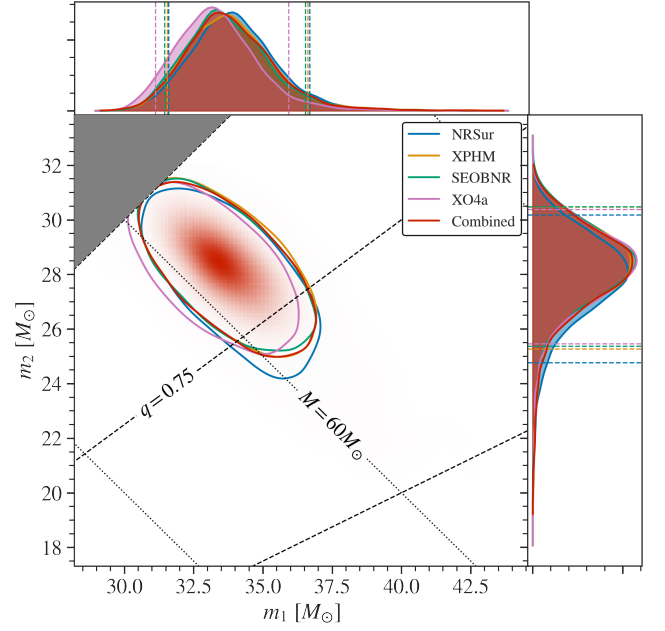


Figure 2. The joint probability distributions for the two component masses, as measured in the source frame using the four indicated waveform models. The shading density indicates the combined posterior, averaging the posterior equally over the four waveform models. Vertical dashed lines in the one-dimensional marginals indicate the 90% credible intervals. The individual component masses of the source are well-measured due to the high SNR, with values given in Table 2.

tion. Samples for individual waveform models are available in the GWTC-4.0 data release (Abac et al. 2025f).

In the source’s rest frame, the system has a chirp mass $\mathcal{M} = 26.8^{+0.9}_{-1.0} M_\odot$, total mass $M = 61.9^{+2.0}_{-2.0} M_\odot$, and components $(m_1, m_2) = (33.7^{+2.9}_{-2.2}, 28.2^{+2.2}_{-3.1}) M_\odot$. The joint posterior distribution of the component masses is shown in Figure 2. We find good agreement in the mass measurements between the waveform models. All waveform models prefer a mass ratio away from the equal mass case, with an overall measurement $q = m_2/m_1 = 0.84^{+0.12}_{-0.14}$.

The luminosity distance was estimated as $D_L = 289^{+183}_{-130}$ Mpc, implying a redshift $z = 0.06^{+0.04}_{-0.03}$ using the cosmological prior described in Ade et al. (2016) and Abac et al. (2025h). The detector-frame masses are related to source-frame masses by a factor of $(1 + z)$. The merger remnant’s detector-frame mass, $M_f^{\text{det}} = 62.7^{+1.5}_{-1.4} M_\odot$, and its final spin $\chi_f = 0.68^{+0.02}_{-0.02}$, determine the frequencies and damping times of the quasi-normal modes (QNMs) (See Section 3 for details).

Given the high SNR of the signal, we are able to constrain the spin vectors of the compact objects well. The best-measured spin parameter χ_{eff} (Santamaria et al. 2010; Ajith & Bose 2009), defined as:

$$\chi_{\text{eff}} = \frac{\vec{\chi}_1 \cdot \hat{L} + q \vec{\chi}_2 \cdot \hat{L}}{1 + q}, \quad (1)$$

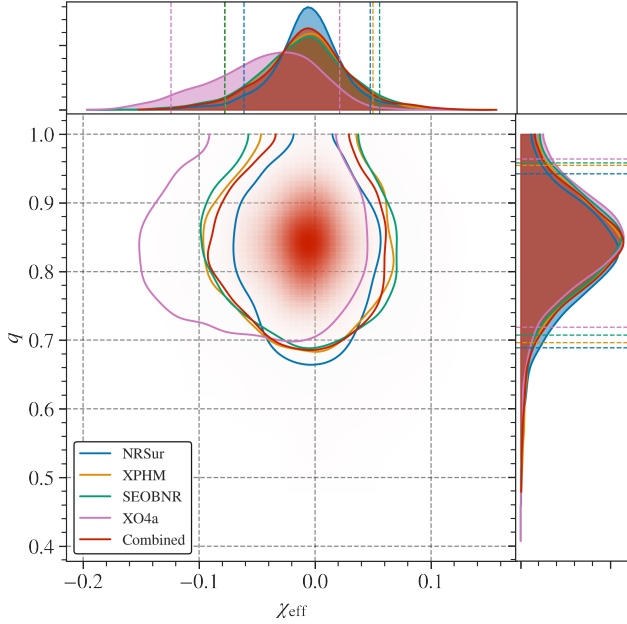


Figure 3. The joint probability distributions for the mass ratio q and effective inspiral spin χ_{eff} . The mass ratio is well constrained away from equal masses, $q < 1$. The signal’s effective inspiral spin is well measured to be $\chi_{\text{eff}} = -0.01^{+0.06}_{-0.07}$ and is not strongly correlated with q .

is strongly constrained to $\chi_{\text{eff}} = -0.01^{+0.06}_{-0.07}$ and bears minimal correlation with the mass ratio as shown in Figure 3. Here, $\vec{\chi}_1$ and $\vec{\chi}_2$ are the dimensionless spin vectors of the primary and secondary compact objects respectively and \hat{L} is the unit orbital angular momentum vector, measured at a reference frequency of 20 Hz.

Figure 4 shows the magnitude of the spin vectors and their tilt angles relative to the orbital angular momentum vector of the system. The magnitudes of the spins are likely small, being constrained at 90% probability to be $\chi_1 < 0.38$, $\chi_2 < 0.50$. The in-plane components of both spin vectors are found to be small and consistent with zero. Consequently, the effective precession parameter χ_p (Schmidt et al. 2015), which captures the dominant contribution from in-plane spins, is similarly constrained to be $\chi_p < 0.42$. Thus, the spin configuration is constrained to the remaining possibility that the spins of the two components are oppositely aligned to each other, with low magnitudes. The spin components aligned with the orbital angular momentum direction are estimated to be $\vec{\chi}_1 \cdot \hat{L} = 0.0^{+0.1}_{-0.2}$ and $\vec{\chi}_2 \cdot \hat{L} = 0.0^{+0.3}_{-0.1}$.

The angle θ_{JN} between the total angular momentum of the system and the line of sight is well-measured (see figure 5), with results favoring edge-on viewing angles over face-on ones. As the signal was observed by only a single detector, sensitive to only one polarization, the entirety of this information must be coming from the relative multipole amplitudes and their differential emission patterns as functions of θ_{JN} . When averaged over the different waveform models, the optimal SNRs $\rho_{\ell,m}$ of the most significant higher order

angular ℓ, m multipoles of the inspiral are $\rho_{2,\pm 1} = 1.3^{+1.4}_{-1.0}$, $\rho_{3,\pm 3} = 2.2^{+1.6}_{-1.6}$, and $\rho_{4,\pm 4} = 3.3^{+0.5}_{-1.7}$ (Mills & Fairhurst 2021). The bound of the $\ell = |m| = 4$ mode SNR away from zero makes this the first CBC with a confident detection of an $\ell = 4$ mode in the signal.

Despite the high SNR, the measurement precision of source intrinsic parameters (masses and spins) is not extraordinarily high in the context of the overall catalog, as longer signals from lower mass sources tend to have more cycles in the sensitive band of the detector (Cutler & Flanagan 1994; Poisson & Will 1995). Likewise, although GW230814 is relatively nearby, lower mass systems have been detected a similar distances with lower SNR.

2.3. Astrophysical context

As the signal was only observed in a single detector, constraints on the sky location from timing information are absent. The remaining information from the prior that favours higher distances make it unlikely that it originated from a direction that corresponds to a lower response in LLO.

PE indicates that the mass parameters of the GW230814 progenitor are consistent with those of the known BBH population (Abbott et al. 2023b). Based on the known population, and the sensitivity of the detectors in O4, one would expect to observe a signal with matched-filter SNR at least as great as that observed for GW230814 in approximately 1% of systems. The signal strength is therefore fully consistent with expectations for a population of the size found in GWTC-4.0 (Abac et al. 2025i).

3. TESTS OF GENERAL RELATIVITY

We present tests of GR with GW230814, extending methods traditionally applied to coherent multi-detector observations—which suppress the impact of instrumental noise (Abac et al. 2025c,d,e)—to a single-detector signal. The performed suite of tests probes the inspiral, ringdown, dispersion, and echoes, as qualitatively shown in Figure 6. While most results are consistent with GR, some outliers arise, particularly in the ringdown, as discussed below.

Of those that showed consistency with expectations, we briefly describe some null results here. We performed a residuals test as described in Abbott et al. (2021a), that involves subtracting the maximum-likelihood XPHM waveform from the data, analysing the residuals using BayesWave (Cornish & Littenberg 2015; Cornish et al. 2021, 2024), and comparing it to a background of detector noise (the null hypothesis). This yields a p-value of 0.85, showing consistency with noise, as under the null hypothesis, the p-values should be uniformly distributed between 0 and 1. A Modified Dispersion Relation (MDR) test (Mirshekari et al. 2012) was conducted to probe the possibility of dispersion effects on the signal as it travels from the source to the detector. The results of this test are also consistent with GR. Finally, searches for both modelled (Uchikata et al. 2019; Lo et al. 2019) and unmodelled (Tsang et al. 2018) late-time echoes were performed, with neither of these searches find any statistically significant evidence for echoes.

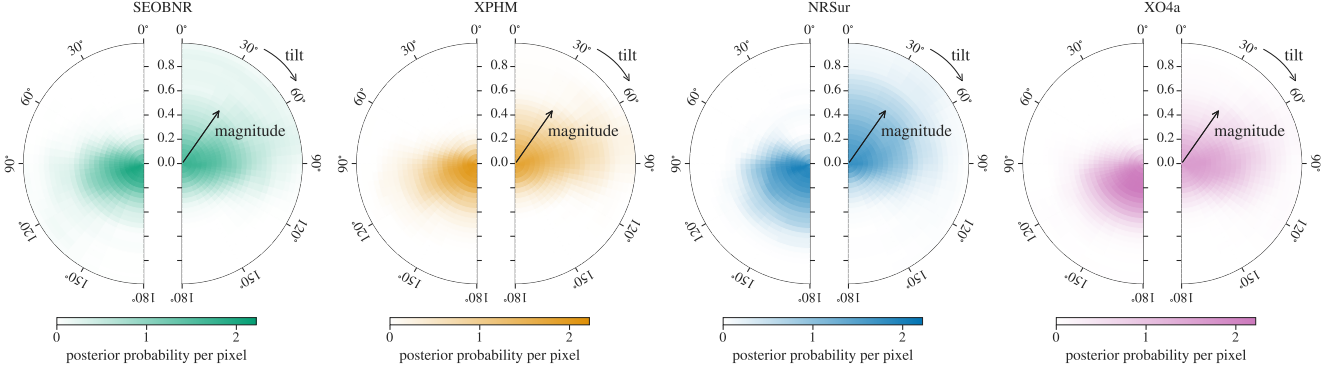


Figure 4. The joint posterior probability density estimates for the magnitude and tilt angle of the spin vectors of the source, obtained using the four indicated waveform models at a reference frequency of $f_{\text{ref}} = 20$ Hz. The left and the right semicircles in each panel show the spins of the primary and secondary component objects, respectively. For all models, the spin vectors are constrained to have small magnitudes. The small value of χ_{eff} further implies that they are oppositely aligned along the direction of the orbital angular momentum.

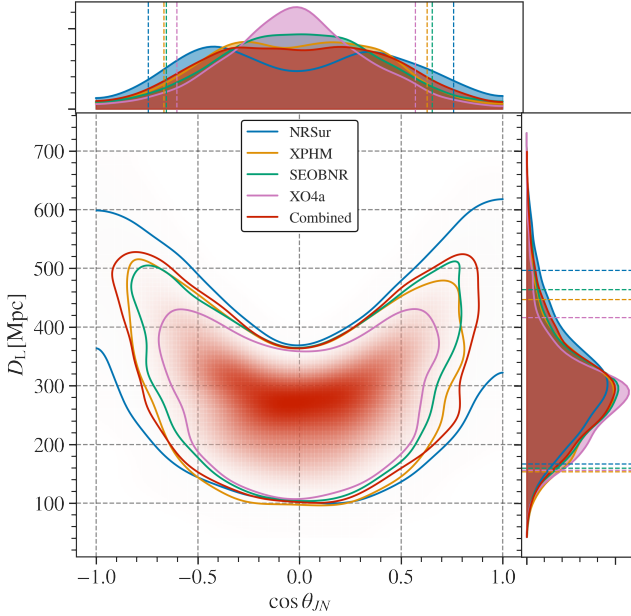


Figure 5. The joint posterior probability distribution for the cosine of the angle between the line of sight and the total angular momentum of the binary $\cos \theta_{JN}$ at a reference frequency of 20 Hz, and the luminosity distance to the source D_L . These analyses rule out a face-on or face-off configuration at high credibility (the prior on $\cos \theta_{JN}$ is flat). At these signal strengths, despite the fact that a single detector cannot constrain the polarization of the signal, the information on the viewing angle is provided by the sub-dominant angular modes in the waveform. Credible intervals are given in Table 2.

3.1. TIGER / FTI / PCA

Tests of the inspiral part of the waveform are performed by both the Flexible Theory-Independent (FTI) (Mehta et al. 2023) and Test Infrastructure for GEneral Relativity (TIGER) (Agathos et al. 2014; Meidam et al. 2018; Roy et al. 2025) pipelines. These tests permit deviations from GR

in the non-spinning post-Newtonian (PN) coefficients, with each deviation parameter introduced and sampled independently. The FTI pipeline uses the SEOBNRv5HM_ROM waveform model as its base GR waveform, while TIGER relies on XPHM. The deviations are applied to the non-spinning part of the PN coefficients in GR $\psi_i^{\text{GR,NS}}$, as

$$\psi_i \rightarrow (1 + \delta\hat{\varphi}_i)\psi_i^{\text{GR,NS}} + \psi_i^{\text{GR,S}}, \quad (2)$$

where $\delta\hat{\varphi}_i$ are the deviation parameters and $(\psi_i^{\text{GR,NS}}, \psi_i^{\text{GR,S}})$ are the spin-independent and spin-dependent part of the PN coefficient from GR, respectively. These corrections are applied in the inspiral part of the signal and then turned off when transitioning to the merger-ringdown. FTI and TIGER differ mainly in their choice of cutoff frequency: FTI adopts a higher cutoff, allowing it to probe deeper into the late inspiral and thereby place tighter constraints on the high-order PN coefficients.

The TIGER pipeline additionally modifies coefficients in the intermediate and merger-ringdown parts of the waveform. Parameters $\delta\hat{b}_1, \delta\hat{b}_2, \delta\hat{b}_3, \delta\hat{b}_4$ capture deviations in the numerical relativity (NR)-calibrated coefficients in the intermediate regime, and the parameters $\delta\hat{c}_1, \delta\hat{c}_2, \delta\hat{c}_4, \delta\hat{c}_\ell$ capture deviations in the merger-ringdown calibration coefficients (Roy et al. 2025).

Figures 7 and 8 summarize the results. The inspiral parameters are consistent with GR, with Figure 7 showing 90% upper bounds on the magnitude of deviations. Differences between FTI and TIGER bounds arise primarily from their cutoff frequency choices and reflect the systematic uncertainties associated with modeling. Because the FTI test for GW230814 uses a higher tapering frequency than in earlier implementations, these bounds are not directly comparable with those reported in GWTC-3. In contrast, the bounds from GW170817 (Abbott et al. 2019) remain comparable, as the old and new tapering frequencies lie outside the detectors' sensitive band.

During the inspiral, both FTI and TIGER are consistent with GR (deviation parameters consistent with zero), whereas the TIGER's merger-ringdown parameters $\delta\hat{c}_i$ show

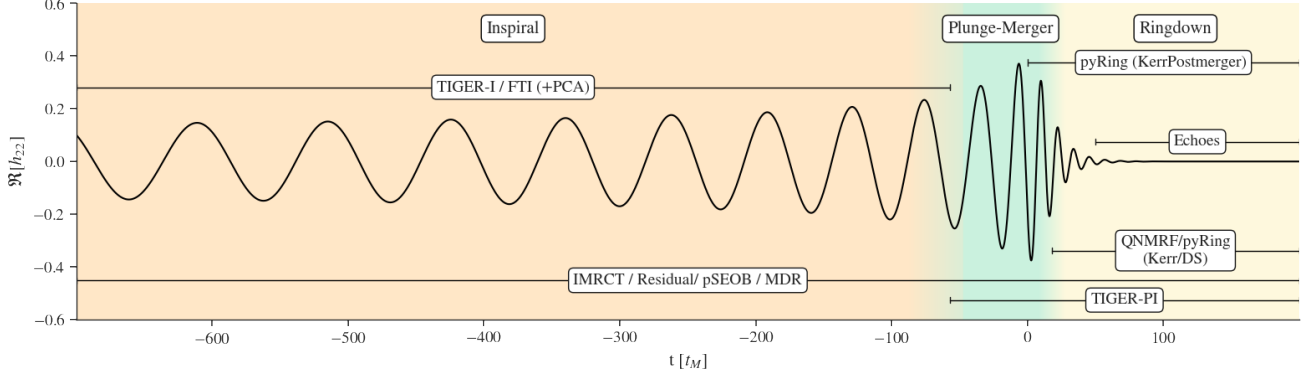


Figure 6. Illustrative $(2,2)$ mode waveform showing the domains of various tests of GR performed on GW230814. The waveform is generated with typical parameters consistent with the posterior and is schematically divided into inspiral (orange), plunge-merger (light green), and ringdown (yellow). Corresponding analysis frameworks include TIGER-I/FTI for inspiral, TIGER-PI for plunge-merger-ringdown, pyRing (KerrPostmerger) for merger-ringdown, QNMRF and pyRing (Kerr/DS) for ringdown, and IMRCT, residual, pSEOBS, and MDR for the full signal. Echo searches are performed in the late ringdown phase.

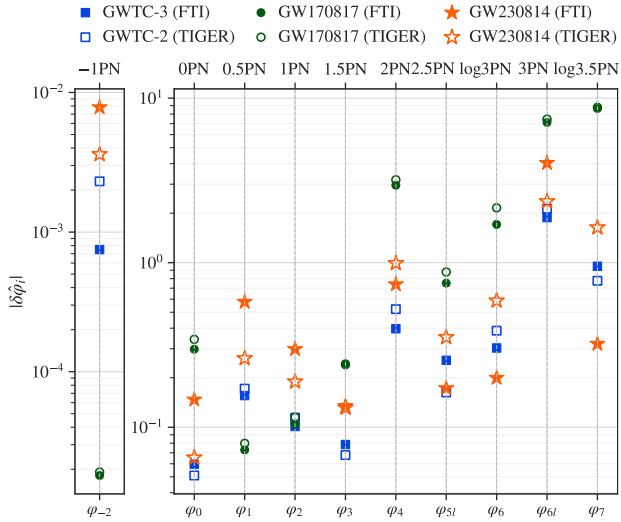


Figure 7. Bounds from the FTI and TIGER tests on the PN coefficients in the inspiral part of the signal. For higher-order PN terms, the bounds improve on similar previously presented constraints from GW170817 (Abbott et al. 2019), and in some cases, are tighter than bounds from the entire GWTC-2 and GWTC-3 populations (Abbott et al. 2021b,a).

posteriors shifted from the GR prediction. The GR quantiles for these coefficients are 1.4%, 2.1%, 4.1%, 0.2% for $\delta\hat{c}_1$, $\delta\hat{c}_2$, $\delta\hat{c}_4$, and $\delta\hat{c}_\ell$, respectively. Despite these shifts, we find no statistically significant evidence for deviations from GR, with \log_{10} Bayes factors, $\log_{10} \mathcal{B}$ ranging from -3 to 0.2 . We note that these values depend on prior choices; in the TIGER pipeline, each deviation parameter is assigned a uniform prior in $[-20, 20]$, chosen conservatively to match the ranges used for quieter signals with broader posteriors.

The FTI and TIGER pipelines vary each deviation parameter separately. To account for possible correlated devia-

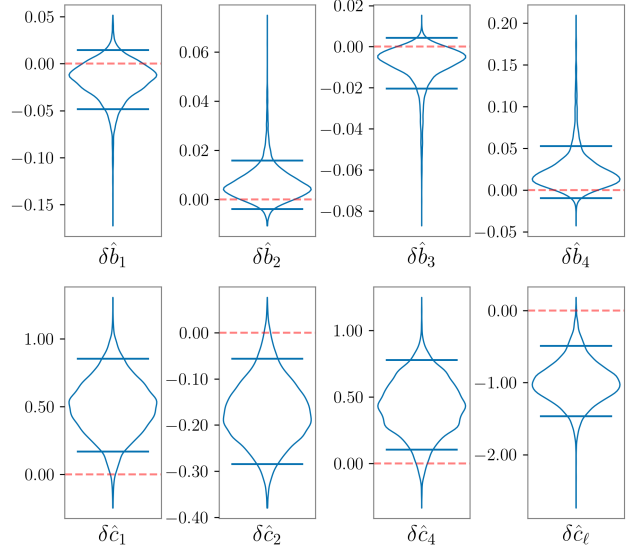


Figure 8. Results from the TIGER test on the intermediate and merger-ringdown part of the signal using the waveform XPHM. The red dashed lines indicate the GR prediction at 0. For the intermediate coefficients $\delta\hat{b}_i$, the GR prediction value of zero lies within the 90% credible intervals, but for the merger-ringdown coefficients, $\delta\hat{c}_i$, the GR prediction lies outside the 90% credible intervals.

tions across the inspiral parameters, starting at 1.5PN order and including up to 3.5PN order, we diagonalize the covariance matrix and identify the leading and sub-leading eigenvectors (linear combinations of the original PN deformation parameters, referred to as Principal Component Analysis (PCA) parameters) that have the smallest eigenvalues (Pai & Arun 2013; Saleem et al. 2022; Shoom et al. 2023). In this parametrization, results for the PCA components from both the TIGER and the FTI frameworks are consistent with GR,

with zero deviation lying within the 90% credible intervals of the posterior.

3.2. Inspiral-Merger-Ringdown Consistency

The Inspiral–Merger–Ringdown Consistency Test (IMRCT) (Hughes & Menou 2005; Ghosh et al. 2016, 2018) compares the consistency of the final mass and spin inferred from the data below and above a frequency cutoff that approximately separates the inspiral and merger–ringdown parts of the signal in the frequency domain. The frequency cutoff of 144 Hz is set to be the innermost circular orbit frequency of the remnant Kerr black hole whose properties are inferred with the entire signal using the XPHM waveform that is used for this test. The SNRs for the signal below and above the cutoff are 35.3 and 21.7.

Figure 9 shows the results of the test in terms of the parameters

$$\frac{\Delta M_f}{\bar{M}_f} = 2 \frac{M_f^{\text{low}} - M_f^{\text{high}}}{M_f^{\text{low}} + M_f^{\text{high}}}, \quad \frac{\Delta \chi_f}{\bar{\chi}_f} = 2 \frac{\chi_f^{\text{low}} - \chi_f^{\text{high}}}{\chi_f^{\text{low}} + \chi_f^{\text{high}}}, \quad (3)$$

where \bar{M}_f and $\bar{\chi}_f$ denote the averages of the final mass and spin estimated from the two parts of the signal analyzed separately. Following Abbott et al. (2021a), we also reweigh the IMRCT posteriors in the final mass and spin deviation parameters to account for the non-uniform priors induced by the mapping from uniformly sampled component masses.

The results appear consistent with the GR prediction of (0,0), which is contained within the 47% contour. This indicates IMRCT is not sensitive to the anomaly found by TIGER in the merger-ringdown. The credible region is comparable in size to that for the entire population in the third Gravitational-Wave Transient Catalog (GWTC-3.0) (Abbott et al. 2021a).

3.3. pSEOBNR

The pSEOBNRv5PHM (pSEOBNR) analysis (Brito et al. 2018; Ghosh et al. 2021; Maggio et al. 2023; Toubiana et al. 2024; Pompili et al. 2025) introduces fractional deviations $\delta \hat{f}_{\ell m 0}$ and $\delta \hat{\tau}_{\ell m 0}$ in the frequency and damping time of the dominant QNMs in the ringdown portion of the SEOBNR waveform as:

$$f_{\ell m 0} = f_{\ell m 0}^{\text{GR}}(1 + \delta \hat{f}_{\ell m 0}), \quad \tau_{\ell m 0} = \tau_{\ell m 0}^{\text{GR}}(1 + \delta \hat{\tau}_{\ell m 0}), \quad (4)$$

where the GR values depend on the remnant’s mass and spin (Stein 2019), which are inferred from the progenitor binary’s properties via NR fits (Jiménez-Forteza et al. 2017; Hofmann et al. 2016). The indices ($\ell m n$) label the QNM angular harmonics (ℓm) and overtones ($n = 0$ being fundamental). This approach employs the full signal length and SNR as pSEOBNR modifies these parameters within a full inspiral–merger–ringdown (IMR) model. The present analysis targets deviations in the (2,2,0) QNM by jointly sampling over $(\delta \hat{f}_{220}, \delta \hat{\tau}_{220})$, along with the standard BBH parameters. For the QNM deviation parameters, we use uniform priors in the

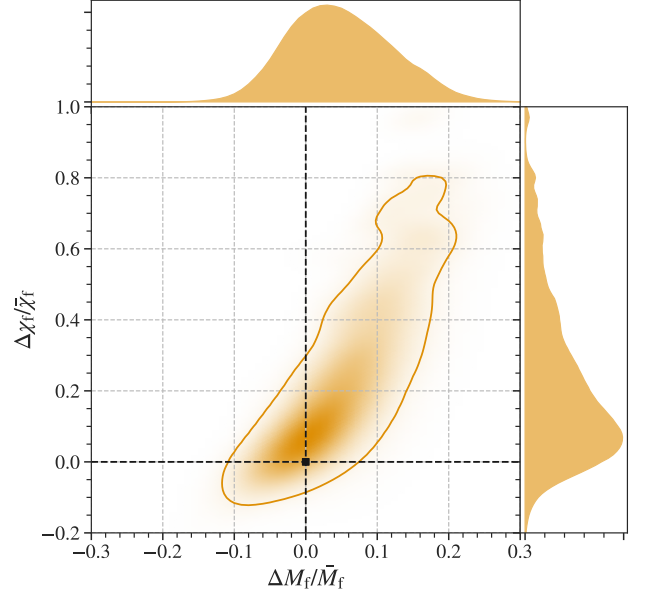


Figure 9. Results from the IMRCT using the waveform XPHM. The black square denotes the GR prediction at $\bar{M}_f = \bar{\chi}_f = 0$. The GR parameters of the lower-frequency and higher-frequency parts of the signal are seen to be consistent with this test.

ranges $\delta \hat{f}_{220} = [-0.8, 2.0]$ and $\delta \hat{\tau}_{220} = [-0.8, 2.0]$. The other modes included in the model, but not modified, are the (2,1,0), (3,3,0), (3,2,0), (4,4,0), (4,3,0) and (5,5,0) (Pompili et al. 2023).

The results of the analysis of GW230814 are summarized in Figure 10, which shows the 90% credible levels of the posterior probability distribution of the fractional deviations in the frequency and damping time of the (2,2,0) QNM, and their corresponding one-dimensional marginalized posterior distributions. The data support a damping time smaller than expected from GR. The bounds from the pSEOBNR analysis are $\delta \hat{\tau}_{220} = -0.3^{+0.15}_{-0.12}$, with a GR quantile of $1 - \text{CI}(\delta \hat{f}_{220} = \delta \hat{\tau}_{220} = 0) = 0.0092$ where CI denotes the credible interval. Bayesian model selection between the pSEOBNR and SEOBNR models results in a $\log_{10} \mathcal{B}$ of -0.43 between the two models, indicating that the data favours SEOBNR. However, as mentioned before, Bayes factors are sensitive to the choice of prior ranges for the deviation parameters. The credible-level result indicates potential deviations from the GR prediction. The result is in tension with the population constraint from GWTC-3.0, which is $\delta \hat{\tau}_{220} = 0.13^{+0.21}_{-0.22}$ (Abbott et al. 2021a).

The measured frequency and damping time from the pSEOBNR result are shown in Figure 11, in comparison with results from other analyses described below. The IMRCT and residuals test mentioned earlier, being broadband in nature, may not be as sensitive as pSEOBNR to specific deviations in the waveform. The consistency between the pSEOBNR and other results is further strengthened by running the TIGER and IMRCT pipelines on the maximum-likelihood waveform from the pSEOBNR analysis. These tests yield similar re-

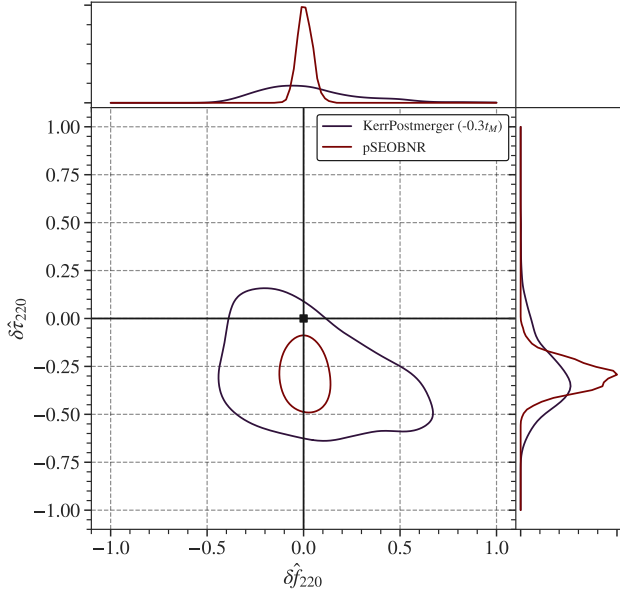


Figure 10. The 90% credible regions for the posterior probability distribution of the fractional deviations in the frequency and damping time of the $(2, 2, 0)$ QNM, $(\delta\hat{f}_{220}, \delta\hat{\tau}_{220})$ for GW230814. The contours and corresponding marginalized posteriors are shown for the pSEOBNR (dashed–dotted maroon, see Section 3.3) and pyRing KerrPostmerger (solid black, see Section 3.4) analyses. The black square denotes the GR prediction of $\delta\hat{f}_{220} = \delta\hat{\tau}_{220} = 0$.

sults to the actual signal, with TIGER finding the deviation and IMRCT not.

3.4. *pyRing*

pyRing (Carullo et al. 2019, 2025) analyzes the post-merger phase of BBH coalescences using a time-domain likelihood (Carullo et al. 2019; Isi & Farr 2021; Del Pozzo & Nagar 2017). Unlike the pSEOBNR pipeline, it excludes the inspiral portion of the signal. The analysis employs multiple signal models, each suited to different times after merger, with time conveniently expressed in units scaled by the detector-frame final mass, $t_M = GM_f^{\text{det}}/c^3 \simeq 0.31$ ms. To search for possible deviations from GR, the framework allows for parameterized shifts in the Kerr QNM frequencies and damping times, determined by the final detector-frame mass and spin of the remnant black hole (BH).

We adopt the median of the posterior of the invariant strain peak defined as:

$$t_{\text{peak}} = \max_t \sqrt{\sum_{\ell, m} |h_{\ell m}(t)|^2} \quad (5)$$

from the NRSur analysis in LLO as our fiducial reference GPS time $t_{\text{LLO}} = 1376089759.805280$ s, and report offsets from this time in mass units t_M .

The most agnostic damped-sinusoid (DS) model represents the ringdown portion of the waveform as a sum of decaying sinusoids with free amplitudes and phases. Since this model

allows for only QNM with time-independent frequencies and damping times, the analysis is started $10 t_M$ after t_{LLO} (Kamaretsos et al. 2012). The Kerr model builds on this by incorporating the frequency structure associated with perturbations of Kerr BHs (Berti & Klein 2014). The KerrPostmerger model (Gennari et al. 2024), includes information about the binary progenitor system, relying on time-dependent amplitudes calibrated to NR simulations, which allow it to fit the entire post-peak data (Damour & Nagar 2014; Del Pozzo & Nagar 2017; Nagar et al. 2020a,b). The model includes the $(\ell, |m|) = (2, 2), (2, 1), (3, 3), (4, 4),$ and $(5, 5)$ angular multipoles, and allows deviations in the frequency and damping time of the $(2, 2)$ mode. Among all signal models, KerrPostmerger is the most sensitive, as it effectively captures the non-linearities, overtone excitations, and transient features near the merger, allowing for the most detailed extraction of information from the post-merger signal, starting at the peak of the $(2, 2)$ invariant strain.

Results from the DS model containing a single sinusoid component starting at $10 t_M$ after t_{LLO} yield a measurement of frequency $f = 246_{-32}^{+24}$ Hz and damping time $\tau = 2.80_{-0.82}^{+1.27}$ ms. These results are illustrated in Figure 11. Using the remnant properties estimated from the NRSur IMR analysis, the predicted QNM frequencies and damping times can be computed for a subset of modes and compared to these agnostic measurements. The frequency and damping time of the DS do not completely overlap with those of the $(\ell, m, n) = (2, 2, 0)$ Kerr fundamental mode of a remnant black hole with properties inferred from our IMR analysis. Instead, the median frequency of the DS lies between those of the $(2, 2, 0)$ and $(2, 1, 0)$ modes, as shown in Figure 11.

Using the Kerr model, with the $(2, 2, 0)$ and $(2, 1, 0)$ modes included, we find that the damping time is reduced relative to the single DS, and is closer to the results from the pSEOBNR analysis. The frequencies inferred for the individual modes are set by the common M_f^{det} and χ_f parameters in the model, and are consistent with the IMR result, however the damping times show a lower than expected value.

Results for the KerrPostmerger model, which analyses data from times before the damped sinusoid model, are also shown in Figure 11. The frequency and damping time for the KerrPostmerger model also do not completely overlap with those of the $(2, 2, 0)$ Kerr fundamental mode of a remnant black hole with properties inferred from our IMR analysis. This time, the damping time lies largely below that of the $(2, 2, 0)$ mode, consistent with the finding from the pSEOBNR analysis, although the 90% credible region is somewhat larger. The discrepancy between the GR prediction and the KerrPostmerger fit is quantified by the deviation parameters $\delta\hat{\tau}_{220}$ and $\delta\hat{f}_{220}$, with 90% credible interval shown in Figure 10. Bayesian model selection between the KerrPostmerger model with deviation parameters allowed to vary in the range $\pm 100\%$ and the same model with $\delta\hat{\tau}_{220} = \delta\hat{f}_{220} = 0$ yield a $\log_{10} \mathcal{B}$ of 1.9 in favour of the GR model.

3.5. QNM Rational Filter

The Quasi-Normal Mode Rational Filters (QNMRFs) pipeline (Ma et al. 2022, 2023a,b; Lu et al. 2025a) analyzes the post-merger signals from BBH coalescences by applying a frequency-domain filter to remove signal components with specific complex-valued frequencies. This approach can eliminate one or more QNMs corresponding to a given remnant BH mass M_f^{det} and spin χ_f from the ringdown signal. The filtered waveform is then transformed back to the time domain and analyzed using the same time-domain likelihood formalism as described in Section 3.4. Since the filters remove DSs or QNMs without requiring prior knowledge of their amplitudes or phases, the likelihood function remains two-dimensional regardless of the number of modes removed. The QNMRFs analysis adopts the same starting-time convention as that in Section 3.4 with the same t_M and t_{LLO} values.

The results from the QNMRFs pipeline, when removing a single damped sinusoid at $10t_M$ after t_{LLO} , are shown in Figure 11 and are in close agreement with the pyRing single DS results. Both methods find that the frequency and damping time inferred from the event lie between those of the (2,2,0) and (2,1,0) modes predicted by the IMR inference.

4. INVESTIGATION OF APPARENT DEVIATION FROM GENERAL RELATIVITY

The results presented in the previous section indicate that the inspiral phase of GW230814 is consistent with the predictions of GR. In contrast, the pSEOBNR and TIGER analyses find that deviation parameters that affect the merger-ringdown portion of the signal have posterior probability distributions that are peaked away from the GR value of zero. A non-zero value for a GR deviation parameter does not necessarily imply a violation of GR has been detected. Such deviations have been observed in tests before (Abbott et al. 2021b,a; Maggio et al. 2023) and can be caused by a variety of known effects (Gupta et al. 2024).

A natural starting point to investigate the origin of these potential deviations is to examine the data directly, by comparing the whitened strain with the predictions of the various waveform models employed in the analyses. Figure 12 shows the whitened waveform posteriors for GW230814 derived using the NRSur, XO4a, XPHM, SEOBNR and pSEOBNR models along with the whitened time domain data. While the four GR models yield mutually consistent reconstructions, the pSEOBNR model provides a visibly better fit to the data, particularly near $t - t_{\text{LLO}} = 9$ ms. At this time, the amplitude of the data appears to be lower than predicted by GR-based models. In parameterized frameworks, such a discrepancy would manifest as a reduced damping time τ , a trend that is indeed observed in both the pSEOBNR and pyRing (KerrPostmerger) analyses.

We can confirm this by investigating the contribution to the $\delta\hat{\tau}_{220}$ inference as a function of time by evaluating the integrand of the Fisher information matrix element in the time domain. This is shown in Figure 13 for an analysis starting

at $t - t_{\text{LLO}} = 10t_M$. The Fisher information is

$$I_\tau = \sum_{ij} \frac{\partial h_i}{\partial \tau} C_{ij}^{-1} \frac{\partial h_j}{\partial \tau} = \sum_i \left(\frac{\partial \tilde{h}_i}{\partial \tau} \right)^2, \quad (6)$$

where

$$h_i = A \exp\left(-\frac{t_i}{\tau}\right) \cos(2\pi f t_i) \quad (7)$$

is the DS model, C is the time-domain covariance matrix derived from the estimated noise power spectral density used for the PE analysis (Isi & Farr 2021), and $\tilde{h} = L^{-1}h$ with $C = LL^T$ is the whitened waveform. For illustrative purposes, we choose $f = 250$ Hz and $\tau = 3.5$ ms, consistent with the estimated DS parameters from the ringdown analysis (see Figure 11). For these fiducial parameters, the Fisher information about the parameter τ accumulates rapidly during the time corresponding to the residual deviation at $t - t_{\text{LLO}} = 9$ ms discussed above and shown in Figure 12. The inferred damping time in a DS ringdown analysis is thus particularly sensitive to the data around the time of deviation shown in Figure 12.

This observation then raises a key question: what causes this deviation? The following sections explore whether the feature could be attributed to additional subdominant modes in the ringdown, gravitational lensing of the signal, systematic errors in our modeling of the GR waveform or detector noise artifacts. While we find subdominant ringdown modes and lensing to be unlikely explanations, both waveform systematics and detector noise could be responsible for the observed deviation.

4.1. Tests for subdominant ringdown modes

To test for additional subdominant ringdown modes we apply the Quasi-Normal Mode Rational Filter (QNMRF) and pyRing independently and compare their results.

To determine the modes present in a ringdown signal, the Quasi-Normal Mode Rational Filter (QNMRF) defines a detection statistic \mathcal{D} that quantifies how well the data supports a given two-mode model over a single-mode model Lu et al. (2025b). In this analysis, we focus on the detection of subdominant ringdown modes by comparing a (2,2,0)-only QNM model to models with a different secondary mode. Specifically, we test for the presence of the (2,2,1), (2,1,0), (2,0,0), (3,2,0), (3,3,0), and (4,4,0) modes. To evaluate the detection statistic, we compute a threshold on \mathcal{D} which corresponds to a statistical significance with a 1% false-alarm probability (FAP). We create 300 injections by adding a single QNM with random properties into the detector noise before and after the trigger time. We then compare the detection statistic of this injection between a two-mode hypothesis (for a specific secondary mode) which is known to be incorrect, and the correct single-mode hypothesis. We find a distribution of detection statistics under the null hypothesis and determine the threshold on \mathcal{D} which corresponds to a 1% FAP. This threshold is then compared to the detection statistic computed from the event which is evaluated at multiple start times $t - t_{\text{LLO}}$ since the start time of the stationary

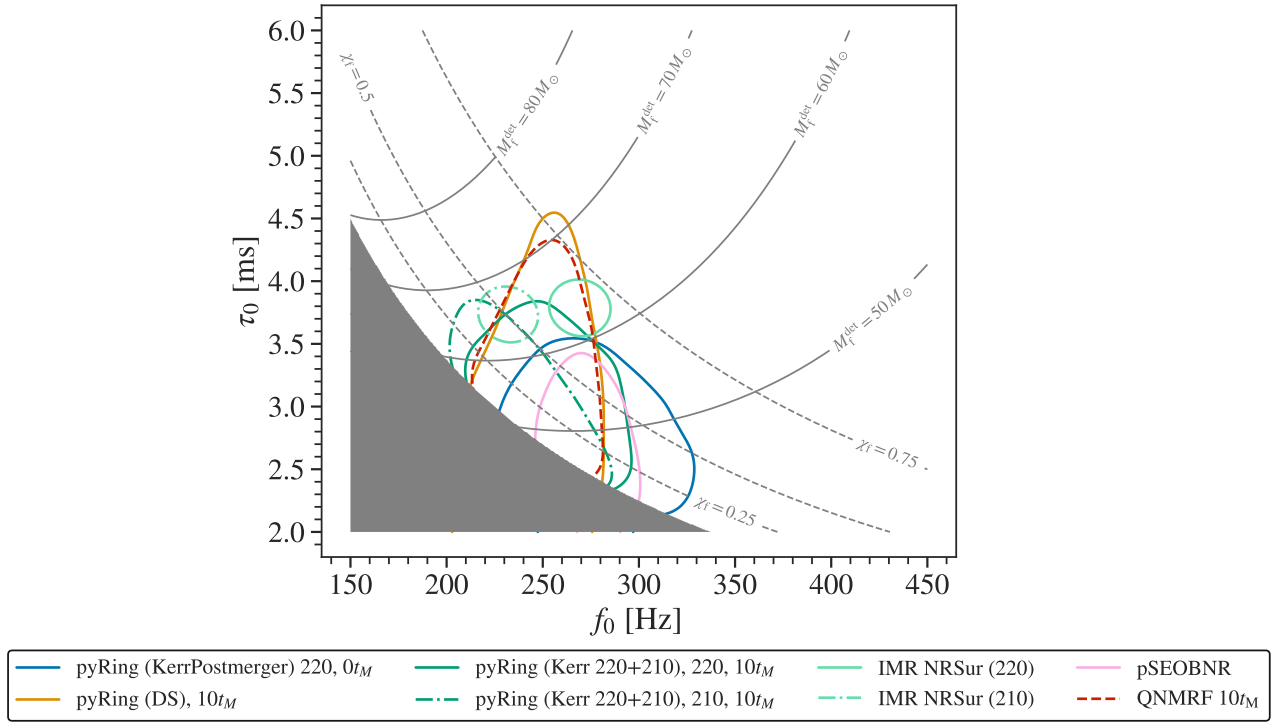


Figure 11. Inferred frequencies and damping times of DSs or modes from models discussed in the text, see section 3. The light gray lines show the frequency and damping time of the $(2, 2, 0)$ fundamental mode of a Kerr black hole at various masses and spins. The dark gray region corresponds to the frequencies and damping times that are inconsistent with a Kerr $(2, 2, 0)$ fundamental mode. The light green solid and dashed curves show the frequency and damping time of the Kerr $(2, 2, 0)$ and $(2, 1, 0)$ fundamental modes for the remnant properties measured in our IMR analysis with the NRSur waveform model. We show results from an analysis using the pSEOBNR (Section 3.3) model in pink. The inferred frequency and damping time of the $(2, 2, 0)$ fundamental mode in this analysis (also shown in Figure 10) are inconsistent with the same mode using estimates of the remnant properties our IMR analysis. Analysis of the post-peak signal starting at $t \sim 10 t_M$ using the pyRing pipeline with a single DS (Section 3.4) is shown in dark orange. The frequency from this analysis spans those inferred by the IMR analysis for the $(2, 2, 0)$ and the $(2, 1, 0)$ modes, and the damping time is consistent with lower values. Analysis with the Kerr model, using both the $(2, 2, 0)$ and the $(2, 1, 0)$ modes is shown in dark green, and shows that assuming the two modes are present in the signal finds a lower damping time, more consistent with the pSEOBNR result. Analysis of the post-peak signal using the KerrPostmerger model (Section 3.4) starting at $t = 0 t_M$ are shown in blue. This model also finds a frequency and damping time for the $(2, 2, 0)$ Kerr fundamental mode that are in tension with the IMR results. Analysis of the post-peak signal starting at $t \sim 10 t_M$ using the QNMRF (Section 3.5) to remove a single damped sinusoid is shown in red and shows close agreement with the pyRing single DS model.

ringdown regime is uncertain. The results of the QNMRF analysis are shown in Figure 14. No two-mode hypothesis is detected with a detection statistic larger than its corresponding threshold at any analysis start time.

The pyRing pipeline also compares the evidence of models with a single DS or with two DSs. The results of model selection for the presence of selected secondary modes vs the $(2, 2, 0)$ mode for the KerrBH model, and for the uninformed DS model, are shown in Figure 14. The Bayesian evidence slightly disfavors models with two DS in the data rather than one with a $\log_{10} \mathcal{B} \sim -0.4$, with the KerrBH model finding

similar results for its most probable secondary modes. This is consistent with the result found by QNMRF; the data do not require the presence of a second ringdown mode.

4.2. Tests for gravitational lensing

Distortions of the GW signal caused by gravitational lensing can masquerade as violations of GR and they must be separately ruled out as a possible cause of apparent GR deviations (Gupta et al. 2024; Mishra et al. 2024). To test for single-image lensing, investigations were performed on GW230814 using two pipelines: GOLUM (Janquart et al.

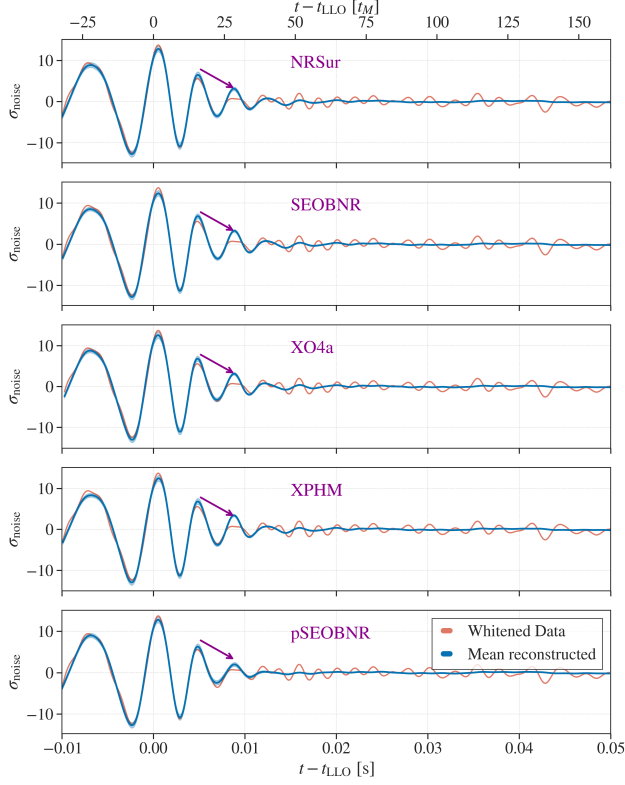


Figure 12. Comparison of whitened data and reconstructed waveforms. The shaded bands around the mean encompass 90% of the waveforms reconstructed from the posterior distribution. The first four panels show the four named GR waveforms, whereas the fifth shows the non-GR pSEOBNR waveform. The additional freedom in the pSEOBNR waveform enables it to better capture features in the data compared to the four GR waveforms, most notably by producing a quicker than expected amplitude decay. This is particularly notable at the time indicated by the arrows, $t - t_{\text{LLO}} \approx 0.085$ s, where the GR waveforms all deviate noticeably from the data and consistently predict a higher than observed strain. This feature may be explained by a random fluctuation in the detector noise; similar fluctuations can be observed at later times (e.g., after $t - t_{\text{LLO}} = 0.04$ s, when no remaining detectable signal is expected).

2021a) and Gravelamps (Wright & Hendry 2021; Liu et al. 2023).

The GOLUM pipeline searches for strong-lensing signatures caused by distortions in the waveform from high-mass lenses (Janquart et al. 2021a). This type of lens causes the formation of multiple images of the same GW, with a magnification, a time delay, and a phase shift n_j of either 0, 0.5, or 1.0 (type-I, II, and III images, respectively) (Ezquiaga et al. 2021). For single GWs such as GW230814, the pipeline searches for phase shifts of $n_j = 0.5$, which can indicate lensing (Janquart et al. 2021b; Wright et al. 2025).

The GOLUM pipeline’s search for type-II images retrieves Bayes factors of $\log_{10} \mathcal{B}_{\text{I}}^{\text{II}} = -1.2$ and $\log_{10} \mathcal{B}_{\text{III}}^{\text{II}} = -1.1$ indicating that a type-II image is disfavored. Since the ex-

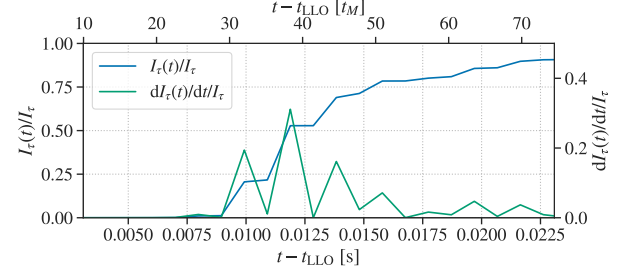


Figure 13. The accumulation of Fisher information about the $\delta\tau_{220}$ parameter over time (partial sums in blue and terms in the sum in green from the final term in Eq. 6) for a DS model with $f = 250$ Hz and $\tau = 3.5$ ms, starting at $t - t_{\text{LLO}} = 10t_M$. Each peak of the green curve corresponds to a peak or trough of the waveform shown in Figure 12, with the highest peak corresponding to the cycle of the signal indicated by the purple arrow in that figure. A DS analysis in the time domain is thus particularly sensitive in its damping time estimate to the times that seem to drive the deviation identified in the pSEOBNR analysis at $t - t_{\text{LLO}} = 9$ ms.

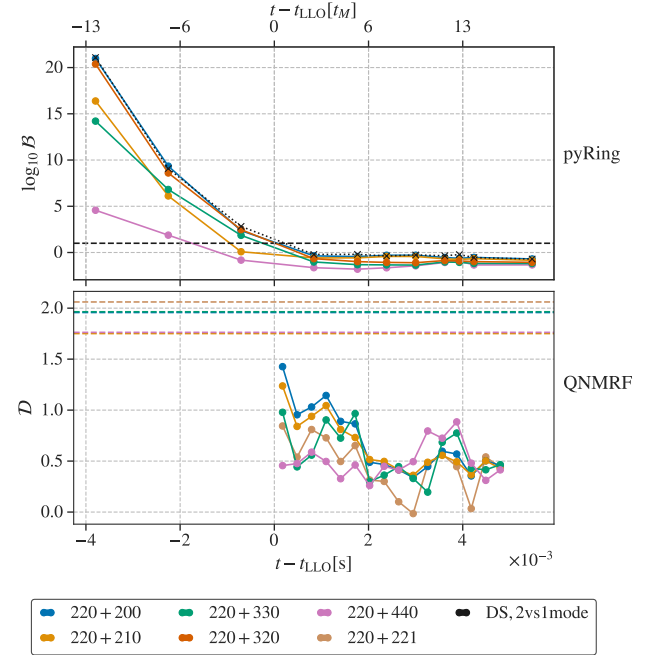


Figure 14. The \log_{10} Bayes factors ($\log_{10} \mathcal{B}$) and detection statistics (\mathcal{D}) from the Kerr and DS pyRing pipelines (top) and the QNMRF pipeline (bottom), quantifying the consistency of the data with the presence of a secondary mode at various starting times. None of the pyRing analyses provide evidence for a secondary mode, as all yield $\mathcal{B} < 10$ (dashed black line) for times beyond t_{LLO} . Similarly, QNMRF does not identify any two-mode combination beyond 220 that meets a FAP threshold of 1% (dashed colored lines).

pectation for standard waveforms is a $\log_{10} \mathcal{B}$ of zero (Vijaykumar et al. 2023), the disfavoring of a type-II image could be a result of either higher-order modes or other alternative deviations in the waveform that break the phase degeneracy (Wright et al. 2025).

The Gravelamps pipeline searches for waveform distortions in a single GW signal arising due to microlensing (Wright & Hendry 2021; Liu et al. 2023). In general, a full wave-optics treatment is needed, analysed using a physical modelling approach with specific associated lens models. This manifests as a single signal with frequency-dependent modulations. In some cases, geometric-optics approximation can be applied. Here, the multiple images overlap and their effect manifests as a single signal with a beating pattern. The physical modelled search with an isolated point-mass yielded a $\log_{10} \mathcal{B}$ of -0.6 . Thus, this signal is not considered as a candidate microlensed event.

4.3. Assessing waveform systematics

Waveform systematics arise from limitations in our GR models, and may cause apparent deviations from GR in our tests against real signals. Waveform systematics are particularly concerning in the case of signals with large SNRs, as in GW230814. While GR-consistent waveform models generally produce similar posterior distributions (see Section 2), subtle differences in the waveforms can become significant when additional degrees of freedom are introduced, potentially mimicking violations of GR (Gupta et al. 2024).

4.3.1. Numerical-relativity (NR) simulations

Assuming that GR signals are well captured by NR simulations, we assess the faithfulness of waveform models against NR data within the relevant parameter space for GW230814.

We run a NR simulation of a BBH system with parameters similar to the maximum-likelihood parameters of the sampled posterior produced by the PE carried out using the NRSur waveform model. The simulation is performed using the Spectral Einstein Code (SpEC) developed by the Simulating eXtreme Spacetimes (SXS) collaboration (Boyle et al. 2019; Scheel et al. 2025; SXS 2025), that employs a multi-domain spectral discretization scheme. The reference eccentricity of the initial data is reduced to $\sim 5 \times 10^{-4}$. The waveform is post-processed, wherein it is extrapolated to infinity using *scri* (Boyle et al. 2020) and corrected for the centre-of-mass drift (Woodford et al. 2019). The resulting waveform has about 42 inspiral cycles. We simulate at three different resolutions to test the convergence, finding that at least all modes up to $\ell = 4$ exhibit convergence of root-mean-square deviations between neighboring resolutions. Furthermore, we project the NR waveforms at different resolutions onto the detector with extrinsic parameters close to the maximum likelihood sample of the NRSur analysis, and find the overlap (without a phase alignment) between the two highest resolutions to be $> 99.998\%$.

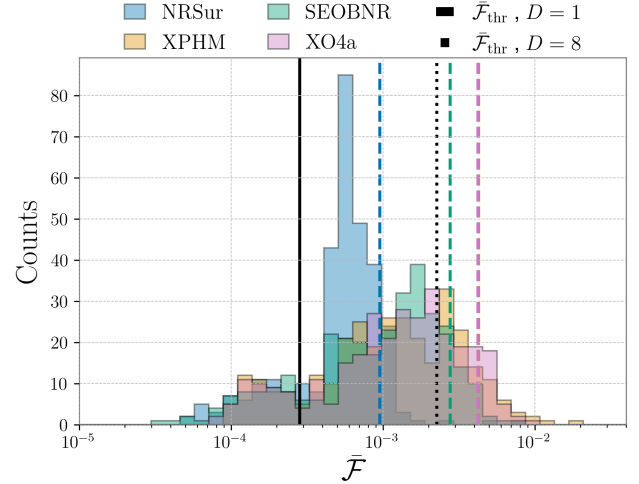


Figure 15. Sky-maximized, SNR-weighted unfaithfulness of the NRSur, SEOBNR, XPHM and XO4a waveform models with respect to 53 simulations (52 from the LVK NR-SXS catalog and the targeted simulation produced as part of this work) compatible with the parameters of GW230814, marginalized over six values of inclination. The NRSur model is the most faithful, with $> 99\%$ of the simulations having unfaithfulness below the threshold of 2.3×10^{-3} required by the SNR of the event (dotted black line).

The accuracy requirements of waveform models can be formulated in terms of the faithfulness \mathcal{F} of the models to the true signal (Lindblom et al. 2008; Damour et al. 2011; Chatziioannou et al. 2017; Toubiana & Gair 2024). Following Chatziioannou et al. (2017), the faithfulness threshold \mathcal{F}_{thr} above which waveform systematics do not affect the results of an analysis is $\mathcal{F}_{\text{thr}} = 1 - D/(2\rho^2)$, or equivalently, $\bar{\mathcal{F}}_{\text{thr}} = D/(2\rho^2)$ where $\bar{\mathcal{F}} = 1 - \mathcal{F}$ is the unfaithfulness and D is the number of intrinsic parameters of the source and ρ is the optimal SNR. For GW230814, $D = 8$ (the two masses and 6 spin components of the two BHs) and $\rho \approx 42$, yielding $\bar{\mathcal{F}}_{\text{thr}} \approx 2.3 \times 10^{-3}$. Alternatively, a more conservative threshold can be computed assuming $D = 1$ (Damour et al. 2011), i.e. $\bar{\mathcal{F}}_{\text{thr}} \approx 3 \times 10^{-4}$. We consider six inclination angles $\iota \in (0, \pi/2)$ and compute the sky-maximized, SNR-weighted unfaithfulness (Pratten et al. 2021; Harry et al. 2018), averaging over four effective-polarization angles and four reference phases. Similar to GW231123 (Abac et al. 2025j), the unfaithfulness is further minimized over an in-plane rotation of the component spins.

Using this statistic, we compare the targeted NR waveform to the NRSur, SEOBNR, XPHM and XO4a models. We find $\bar{\mathcal{F}}$ to be 8.1×10^{-4} , 2.2×10^{-3} , 2×10^{-3} and 2.6×10^{-3} respectively, averaging over the six inclination angles. Expanding the investigation to nearby areas of the parameter space, from $\mathcal{O}(1700)$ SXS simulations in the LVK NR catalog we identify 52 that lie within the 90% credible ranges of mass ratio q , effective inspiral spin χ_{eff} , and precession parameter χ_p for this event. These results are shown in Figure 15. We find that in this region of the parameter space the

NRSur model is the most accurate with respect to the simulations considered, followed by the SEOBNR, XPHM, and XO4a models. With respect to the accuracy requirements considered, the NRSur model satisfies the $D = 8$ threshold for more than 99% of the systems, and the $D = 1$ threshold for $\sim 17\%$ of the systems. Overall, these results indicate that waveform systematics could be a contributing factor for the apparent GR deviation.

4.3.2. Zero-noise waveform injections

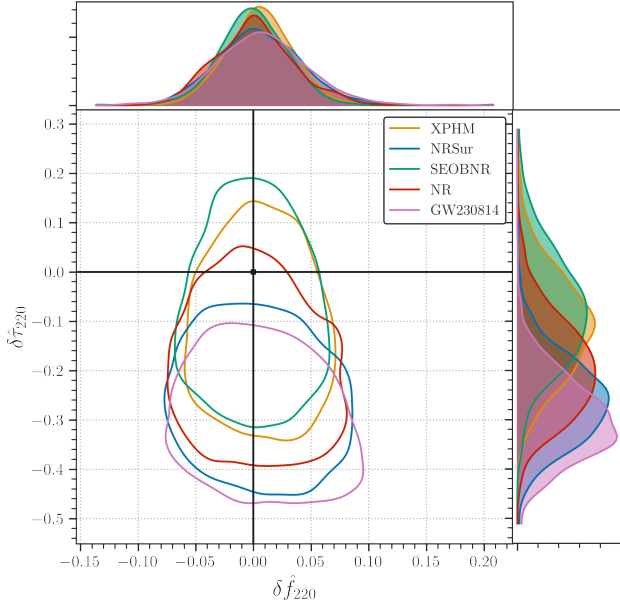


Figure 16. Comparison of the pSEOBNR analyses on injections in zero noise of maximum-likelihood waveforms from different waveform models. The SEOBNR and XPHM injections are recovered consistent with GR. The NRSur and NR injections show a deviation more similar to the one found for the actual signal (in pink).

The accuracy thresholds discussed above are sufficient, not necessary, conditions. A model falling short of the threshold may still yield unbiased results for the source parameters, as is observed in the standard SEOBNR and XPHM analyses of Section 2. Furthermore, such criteria provide no information on which parameters are most susceptible to potential biases, and are known to be overly conservative (Pürrer & Haster 2020; Toubiana & Gair 2024; Finch & Moore 2021).

To further investigate the impact of waveform systematics, we perform zero-noise injections using the maximum-likelihood waveforms from the NRSur, SEOBNR, and XPHM models, and the NR injection, and recover them using the pSEOBNR waveform model. Figure 16 presents these results.

The SEOBNR and XPHM injections yield results consistent with GR. However, we observe that the GR value lies at the edge of the 90% credible interval of the $\delta\tau_{220}$ posterior

for both the NR and NRSur injections, a shift resembling that observed in the real data.

To test the robustness of this effect, we conduct 10 additional zero-noise injections using NRSur waveforms drawn from the PE samples of the event, again analyzing them with pSEOBNR. Two of the ten injections show a deviation in the damping-time similar to the GW230814 analysis. The injected parameters are recovered with good accuracy except for the spin magnitudes and tilt angles.

This lends support to the hypothesis that waveform systematics could be contributing to the observed biased recovery of the ringdown damping-time by the pSEOBNR analysis.

4.4. Assessing detector effects

An alternative explanation for the apparent deviations is that they may be caused by fluctuations of the detector noise. No data-quality issues were reported at the time of GW230814, but low-amplitude noise fluctuations may still be present in the data. Noise fluctuations may be broadly classified as fluctuations consistent with a Gaussian distribution, or as low-amplitude non-Gaussian noise that does not pass the threshold for glitch identification (Soni et al. 2025). For example, Figure 12 shows that noise fluctuations of approximately the same amplitude as the feature previously highlighted in the whitened data are also present at later times, after the black hole has settled into a stationary state and the signal has died away. To investigate the impact of noise, we inject GR-waveforms in Gaussian and real noise, and analyse them with our pipelines to determine how often we find results similarly extreme to those found for GW230814.

4.4.1. pSEOBNR injection results

For the pSEOBNR pipeline, the analysis of GW230814 is compared with: (i) ten NRSur injections in zero noise with parameters taken from the analysis of the event with NRSur; (ii) ten SEOBNR injections in Gaussian noise with the maximum-likelihood values of the PE of the event with SEOBNR; (iii) twenty SEOBNR injections in real LLO noise with the maximum-likelihood values from the PE of the event with SEOBNR; (iv) ten NRSur injections in real LLO noise with the maximum-likelihood values from the PE of the event with NRSur.

The results are shown in Figure 17. We find that five real-noise NRSur injections and two real-noise SEOBNR injection display a Bayes factor higher than one of GW230814. For these injections, the posterior quantiles at which GR is found is lower than the one for GW230814. These results indicate that such deviations can occur due to statistical fluctuations in real detector noise.

4.4.2. pyRing injection results

The pyRing pipeline was used to analyse 198 injections of the maximum-likelihood NRSur waveform into the real noise of the LLO detector at various times around the event, using the KerrPostmerger model of the ringdown with δf and $\delta\tau$

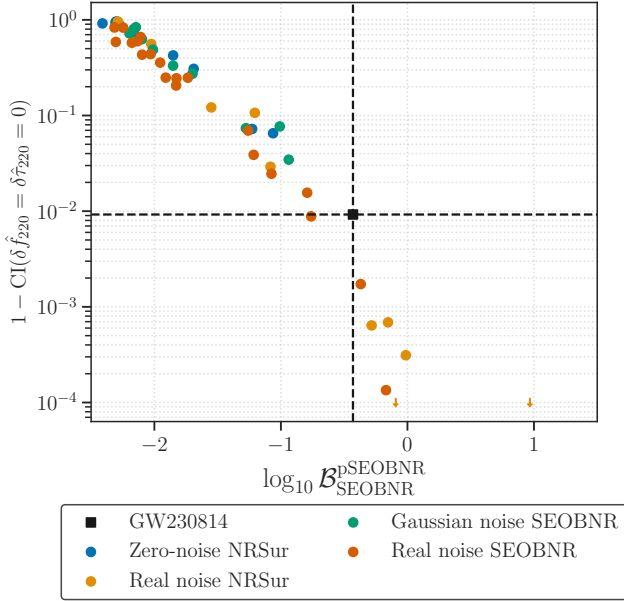


Figure 17. Distribution of $\log_{10} \mathcal{B}_{\text{SEOBNR}}^{\text{pSEOBNR}}$ versus $1 - \text{CI}(\delta \hat{f}_{220} = \delta \hat{\tau}_{220} = 0)$, the posterior exclusion of the GR-consistent values of damping time and frequency from the pSEOBNR pipeline. Shown are results from zero-noise NRSur injections (blue), Gaussian-noise SEOBNR injections (green), and real-noise injections using either SEOBNR (red) or NRSur (yellow). Gaussian noise or waveform systematics alone do not yield Bayes factors as large as GW230814’s. In contrast, real noise, especially when combined with systematics, can reproduce or exceed GW230814’s Bayes factor in 50% of the cases.

parameterised deviations of the (2,2,0) mode enabled. The evidence is compared to that of the same model with no deviations enabled to produce a Bayes factor between this non-GR model and the equivalent GR one. We find a Bayes factor that is greater than that for the observed signal in 59% of cases. Using the same set of simulations, we find credible intervals that are more extreme than those measured for the observed signal in 32% of cases for the damping time and 20% of cases for the frequency. We conclude that the results of the pyRing analysis are consistent with the distribution under noise for similar signals.

5. CONCLUSIONS

GW230814, observed exclusively by the LIGO Livingston detector, exhibits the highest SNR among the signals of GWTC-4.0 (Abac et al. 2025b), which enables tight constraints on its intrinsic parameters. We identify its source as a BBH coalescence, with component masses and spins consistent with the known population of BBH mergers. The strong higher-order modes present in the waveform allow for constraints on the inclination angle, and together with the high SNR enable precise measurement of the mass ratio, despite the absence of a second detector to resolve the full polarization content. These measurements yield well-constrained estimates of the component masses.

Tests of the PN coefficients of the inspiral show consistency with GR, with several constraints from this single signal comparable to population constraints from the whole of GWTC-3.0 Abbott et al. (2021a). However, as shown in Figures 8, 10 and 11 the TIGER, pSEOBNR and pyRing-KerrPostmerger tests reveal mild inconsistencies in the post-inspiral portion of the signal. These deviations are consistent across methods and suggest a reduction in the damping time of the least-damped quasi-normal mode. Figure 12 shows a whitened data segment of the ringdown exhibiting faster amplitude decay than predicted by standard GR templates. Given the limited contribution of this segment to the overall waveform, its impact on GR parameter estimation is expected to be minimal.

We explored several plausible causes of the observed deviations, including subdominant ringdown modes, gravitational lensing, waveform systematics, and detector noise fluctuations. No compelling evidence was found for subdominant modes or lensing effects. We show that similar inconsistencies as observed for GW230814 can be generated for simulated, GR based signals in zero noise and added to both Gaussian noise and, more frequently, real detector noise. Comparable deviations also emerged when analyzing signals with mismatched waveform models, including numerical relativity injections at similarly high SNR.

Most importantly, we cannot exclude statistical noise fluctuations as the cause of these deviations. The lack of data from a second detector severely limits our ability to distinguish between weak non-Gaussian features in the gravitational wave signal and statistical fluctuations in the noise. This underscores the need for a global network of gravitational-wave observatories for robust tests of fundamental physics.

Strain data from the LIGO detectors associated with GW230814 are available from the [Gravitational Wave Open Science Center \(2025\)](#). Samples from posterior distributions of the source parameters, additional materials, and notebooks for reproducing the figures are available on Zenodo ([LIGO Scientific, Virgo, and KAGRA Collaboration 2025](#)).

ACKNOWLEDGMENTS

This material is based upon work supported by NSF’s LIGO Laboratory, which is a major facility fully funded by the National Science Foundation. The authors also gratefully acknowledge the support of the Science and Technology Facilities Council (STFC) of the United Kingdom, the Max-Planck-Society (MPS), and the State of Niedersachsen/Germany for support of the construction of Advanced LIGO and construction and operation of the GEO 600 detector. Additional support for Advanced LIGO was provided by the Australian Research Council. The authors gratefully acknowledge the Italian Istituto Nazionale di Fisica Nucleare (INFN), the French Centre National de la Recherche Scientifique (CNRS) and the Netherlands Organization for Scientific Research (NWO) for the construction and operation of the Virgo detector and the creation and support of the EGO consortium. The authors also gratefully acknowl-

edge research support from these agencies as well as by the Council of Scientific and Industrial Research of India, the Department of Science and Technology, India, the Science & Engineering Research Board (SERB), India, the Ministry of Human Resource Development, India, the Spanish Agencia Estatal de Investigación (AEI), the Spanish Ministerio de Ciencia, Innovación y Universidades, the European Union NextGenerationEU/PRTR (PRTR-C17.11), the ICSC - Centro Nazionale di Ricerca in High Performance Computing, Big Data and Quantum Computing, funded by the European Union NextGenerationEU, the Comunitat Autònoma de les Illes Balears through the Conselleria d'Educació i Universitats, the Conselleria d'Innovació, Universitats, Ciència i Societat Digital de la Generalitat Valenciana and the CERCA Programme Generalitat de Catalunya, Spain, the Polish National Agency for Academic Exchange, the National Science Centre of Poland and the European Union - European Regional Development Fund; the Foundation for Polish Science (FNP), the Polish Ministry of Science and Higher Education, the Swiss National Science Foundation (SNSF), the Russian Science Foundation, the European Commission, the European Social Funds (ESF), the European Regional Development Funds (ERDF), the Royal Society, the Scottish Funding Council, the Scottish Universities Physics Alliance, the Hungarian Scientific Research Fund (OTKA), the French Lyon Institute of Origins (LIO), the Belgian Fonds de la Recherche Scientifique (FRS-FNRS), Actions de Recherche Concertées (ARC) and Fonds Wetenschappelijk Onderzoek - Vlaanderen (FWO), Belgium, the Paris Île-de-France Region, the National Research, Development and Innovation Office of Hungary (NKFIH), the National Research Foundation of Korea, the Natural Sciences and Engineering Research Council of Canada (NSERC), the Canadian Foundation for Innovation (CFI), the Brazilian Ministry of Science, Technology, and Innovations, the International Center for Theoretical Physics South American Institute for Fundamental Research (ICTP-SAIFR), the Research Grants Council of Hong Kong, the National Natural Science Foundation of China (NSFC), the Israel Science Foundation (ISF), the US-Israel Binational Science Fund (BSF), the Leverhulme Trust, the Research Corporation, the National Science and Technology Council (NSTC), Taiwan, the United States Department of Energy, and the Kavli Foundation. The authors gratefully acknowledge the support of the NSF, STFC, INFN and CNRS for provision of computational resources.

This work was supported by MEXT, the JSPS Leading-edge Research Infrastructure Program, JSPS Grant-in-Aid for Specially Promoted Research 26000005, JSPS Grant-in-Aid for Scientific Research on Innovative Areas 2402: 24103006, 24103005, and 2905: JP17H06358, JP17H06361 and JP17H06364, JSPS Core-to-Core Program A. Advanced Research Networks, JSPS Grants-in-Aid for Scientific Research (S) 17H06133 and 20H05639, JSPS Grant-in-Aid for Transformative Research Areas (A) 20A203: JP20H05854, the joint research program of the Institute for Cosmic Ray

Research, University of Tokyo, the National Research Foundation (NRF), the Computing Infrastructure Project of the Global Science experimental Data hub Center (GSDC) at KISTI, the Korea Astronomy and Space Science Institute (KASI), the Ministry of Science and ICT (MSIT) in Korea, Academia Sinica (AS), the AS Grid Center (ASGC) and the National Science and Technology Council (NSTC) in Taiwan under grants including the Science Vanguard Research Program, the Advanced Technology Center (ATC) of NAOJ, and the Mechanical Engineering Center of KEK.

Additional acknowledgements for support of individual authors may be found in the following document:

<https://dcc.ligo.org/LIGO-M2300033/public>.

For the purpose of open access, the authors have applied a Creative Commons Attribution (CC BY) license to any Author Accepted Manuscript version arising. We request that citations to this article use 'A. G. Abac *et al.* (LIGO-Virgo-KAGRA Collaboration), ...' or similar phrasing, depending on journal convention.

The NR simulations were run at the *sonic* High Performance Computing facility at ICTS-TIFR, Bengaluru, India supported by the Department of Atomic Energy, Government of India, under Project No. RTI4001.

Software: The following software was used in this research: Asimov (Williams *et al.* 2023); Astropy (Astropy Collaboration *et al.* 2013, 2018, 2022); BayesWave (Cornish *et al.* 2024); Bilby (Ashton *et al.* 2019; Romero-Shaw *et al.* 2020; Smith *et al.* 2020); Bilby-TGR (Ashton *et al.* 2025); CPNest (Veitch *et al.* 2025); Dynesty (Koposov *et al.* 2024); FTI (Mehta *et al.* 2023); GOLUM (Janquart *et al.* 2021a); GraceDB (GraceDB developers 2023); Gravelamps (Wright & Hendry 2021; Liu *et al.* 2023); GSTLAL (Messick *et al.* 2017; Sachdev *et al.* 2019; Hanna *et al.* 2020; Cannon *et al.* 2020; Sakon *et al.* 2024; Ewing *et al.* 2024; Tsukada *et al.* 2023); GWpy (Macleod *et al.* 2018; Wette 2020); MBTA (Aubin *et al.* 2021); PESummary (Hoy & Raymond 2021); PyCBC (Nitz *et al.* 2024); PyRing (Carullo *et al.* 2019, 2025); PySEOBNR (Mihaylov *et al.* 2025); QNMRF (Ma *et al.* 2022, 2023a,b); Ringdown (Isi & Farr 2021); Spec (Kidder *et al.* 2025); TIGER (Agathos *et al.* 2014; Meidam *et al.* 2018; Roy *et al.* 2025) .

Late in the preparation of this manuscript, an error was discovered in the likelihood evaluation within Bilby (see Talbot *et al.* (2025) and Abac *et al.* (2025h) for details). Consequently, we repeated all GR PE runs and the pSEOBNR analysis using the corrected likelihood. A complete rerun of the simulated signals (including pSEOBNR) and the FTI, TIGER, PCA, and MDR tests was not feasible. However, since the reruns validated that a likelihood reweighting would produce consistent results, a complete rerun was deemed unnecessary. Therefore, we have updated the results from these specific analyses via reweighting, which appropriately corrects the posterior distributions, log-likelihoods, and Bayes factors.

REFERENCES

- Aasi, J., et al. 2015, *Class. Quant. Grav.*, 32, 074001, doi: [10.1088/0264-9381/32/7/074001](https://doi.org/10.1088/0264-9381/32/7/074001)
- Abac, A. G., et al. 2025a, To be published in this issue
- . 2025b, To be published in this issue. <https://arxiv.org/abs/2508.18082>
- . 2025c, To be published in this issue
- . 2025d, To be published in this issue
- . 2025e, To be published in this issue
- . 2025f, To be published in this issue. <https://arxiv.org/abs/2508.18079>
- . 2025g, GW230814 Data Release, Tech. Rep. T2500275. <https://dcc.ligo.org/public/LIGO-T2500275>
- . 2025h, To be published in this issue. <https://arxiv.org/abs/2508.18081>
- . 2025i, To be published in this issue. <https://arxiv.org/abs/2508.18083>
- . 2025j. <https://arxiv.org/abs/2507.08219>
- Abbott, B. P., et al. 2016, *Phys. Rev. Lett.*, 116, 061102, doi: [10.1103/PhysRevLett.116.061102](https://doi.org/10.1103/PhysRevLett.116.061102)
- . 2019, *Phys. Rev. Lett.*, 123, 011102, doi: [10.1103/PhysRevLett.123.011102](https://doi.org/10.1103/PhysRevLett.123.011102)
- . 2020, *Astrophys. J. Lett.*, 892, L3, doi: [10.3847/2041-8213/ab75f5](https://doi.org/10.3847/2041-8213/ab75f5)
- Abbott, R., et al. 2021a. <https://arxiv.org/abs/2112.06861>
- . 2021b, *Phys. Rev. D*, 103, 122002, doi: [10.1103/PhysRevD.103.122002](https://doi.org/10.1103/PhysRevD.103.122002)
- . 2023a, *Phys. Rev. X*, 13, 041039, doi: [10.1103/PhysRevX.13.041039](https://doi.org/10.1103/PhysRevX.13.041039)
- . 2023b, *Phys. Rev. X*, 13, 011048, doi: [10.1103/PhysRevX.13.011048](https://doi.org/10.1103/PhysRevX.13.011048)
- Acernese, F., et al. 2015, *Class. Quant. Grav.*, 32, 024001, doi: [10.1088/0264-9381/32/2/024001](https://doi.org/10.1088/0264-9381/32/2/024001)
- Adams, T., Buskulic, D., Germain, V., et al. 2016, *Class. Quant. Grav.*, 33, 175012, doi: [10.1088/0264-9381/33/17/175012](https://doi.org/10.1088/0264-9381/33/17/175012)
- Ade, P. A. R., et al. 2016, *Astron. Astrophys.*, 594, A13, doi: [10.1051/0004-6361/201525830](https://doi.org/10.1051/0004-6361/201525830)
- Agathos, M., Del Pozzo, W., Li, T. G. F., et al. 2014, *PhRvD*, 89, 082001, doi: [10.1103/PhysRevD.89.082001](https://doi.org/10.1103/PhysRevD.89.082001)
- Ajith, P., & Bose, S. 2009, *Phys. Rev. D*, 79, 084032, doi: [10.1103/PhysRevD.79.084032](https://doi.org/10.1103/PhysRevD.79.084032)
- Alléné, C., et al. 2025, *Class. Quant. Grav.*, 42, 105009, doi: [10.1088/1361-6382/add234](https://doi.org/10.1088/1361-6382/add234)
- Ashton, G., et al. 2019, *Astrophys. J. Suppl.*, 241, 27, doi: [10.3847/1538-4365/ab06fc](https://doi.org/10.3847/1538-4365/ab06fc)
- Ashton, G., Talbot, C., Roy, S., et al. 2025, *Bilby TGR*, v0.2, Zenodo, doi: [10.5281/zenodo.15676285](https://doi.org/10.5281/zenodo.15676285)
- Astropy Collaboration, Robitaille, T. P., Tollerud, E. J., et al. 2013, *A&A*, 558, A33, doi: [10.1051/0004-6361/201322068](https://doi.org/10.1051/0004-6361/201322068)
- Astropy Collaboration, Price-Whelan, A. M., Sipőcz, B. M., et al. 2018, *AJ*, 156, 123, doi: [10.3847/1538-3881/aabc4f](https://doi.org/10.3847/1538-3881/aabc4f)
- Astropy Collaboration, Price-Whelan, A. M., Lim, P. L., et al. 2022, *ApJ*, 935, 167, doi: [10.3847/1538-4357/ac7c74](https://doi.org/10.3847/1538-4357/ac7c74)
- Aubin, F., et al. 2021, *Class. Quant. Grav.*, 38, 095004, doi: [10.1088/1361-6382/abe913](https://doi.org/10.1088/1361-6382/abe913)
- Bécsy, B., Raffai, P., Cornish, N. J., et al. 2017, *Astrophys. J.*, 839, 15, doi: [10.3847/1538-4357/aa63ef](https://doi.org/10.3847/1538-4357/aa63ef)
- Berti, E., & Klein, A. 2014, *Phys. Rev. D*, 90, 064012, doi: [10.1103/PhysRevD.90.064012](https://doi.org/10.1103/PhysRevD.90.064012)
- Boyle, M., Iozzo, D., & Stein, L. C. 2020, *moble/scri: v1.2, v1.2*, Zenodo, doi: [10.5281/zenodo.4041972](https://doi.org/10.5281/zenodo.4041972)
- Boyle, M., et al. 2019, *Class. Quant. Grav.*, 36, 195006, doi: [10.1088/1361-6382/ab34e2](https://doi.org/10.1088/1361-6382/ab34e2)
- Brito, R., Buonanno, A., & Raymond, V. 2018, *Phys. Rev. D*, 98, 084038, doi: [10.1103/PhysRevD.98.084038](https://doi.org/10.1103/PhysRevD.98.084038)
- Cannon, K., et al. 2020. <https://arxiv.org/abs/2010.05082>
- Capote, E., et al. 2025, *Phys. Rev. D*, 111, 062002, doi: [10.1103/PhysRevD.111.062002](https://doi.org/10.1103/PhysRevD.111.062002)
- Carullo, G., Del Pozzo, W., & Veitch, J. 2019, *Phys. Rev. D*, 99, 123029, doi: [10.1103/PhysRevD.99.123029](https://doi.org/10.1103/PhysRevD.99.123029)
- . 2025, *pyRing: a time-domain ringdown analysis python package, 2.7.0*, , Gitlab. <https://git.ligo.org/lscsoft/pyring>
- Chandra, K., Villa-Ortega, V., Dent, T., et al. 2021, *Phys. Rev. D*, 104, 042004, doi: [10.1103/PhysRevD.104.042004](https://doi.org/10.1103/PhysRevD.104.042004)
- Chatziioannou, K., Klein, A., Yunes, N., & Cornish, N. 2017, *Phys. Rev. D*, 95, 104004, doi: [10.1103/PhysRevD.95.104004](https://doi.org/10.1103/PhysRevD.95.104004)
- Chu, Q., et al. 2022, *Phys. Rev. D*, 105, 024023, doi: [10.1103/PhysRevD.105.024023](https://doi.org/10.1103/PhysRevD.105.024023)
- Colleoni, M., Vidal, F. A. R., García-Quirós, C., Akçay, S., & Bera, S. 2025, *Phys. Rev. D*, 111, 104019, doi: [10.1103/PhysRevD.111.104019](https://doi.org/10.1103/PhysRevD.111.104019)
- Cornish, N. J., & Littenberg, T. B. 2015, *Class. Quant. Grav.*, 32, 135012, doi: [10.1088/0264-9381/32/13/135012](https://doi.org/10.1088/0264-9381/32/13/135012)
- Cornish, N. J., Littenberg, T. B., Bécsy, B., et al. 2021, *Phys. Rev. D*, 103, 044006, doi: [10.1103/PhysRevD.103.044006](https://doi.org/10.1103/PhysRevD.103.044006)
- Cornish, N. J., et al. 2024, *BayesWave software*. <https://git.ligo.org/lscsoft/bayeswave>
- Cutler, C., & Flanagan, E. E. 1994, *Phys. Rev. D*, 49, 2658, doi: [10.1103/PhysRevD.49.2658](https://doi.org/10.1103/PhysRevD.49.2658)
- Dal Canton, T., Nitz, A. H., Gadre, B., et al. 2021, *Astrophys. J.*, 923, 254, doi: [10.3847/1538-4357/ac2f9a](https://doi.org/10.3847/1538-4357/ac2f9a)
- Damour, T., & Nagar, A. 2014, *Phys. Rev. D*, 90, 024054, doi: [10.1103/PhysRevD.90.024054](https://doi.org/10.1103/PhysRevD.90.024054)
- Damour, T., Nagar, A., & Trias, M. 2011, *Phys. Rev. D*, 83, 024006, doi: [10.1103/PhysRevD.83.024006](https://doi.org/10.1103/PhysRevD.83.024006)
- Davies, G. S., Dent, T., Tápai, M., et al. 2020, *Phys. Rev. D*, 102, 022004, doi: [10.1103/PhysRevD.102.022004](https://doi.org/10.1103/PhysRevD.102.022004)

- Davies, G. S. C., & Harry, I. W. 2022, *Class. Quant. Grav.*, 39, 215012, doi: [10.1088/1361-6382/ac8862](https://doi.org/10.1088/1361-6382/ac8862)
- Davis, D., Trevor, M., Mozzon, S., & Nuttall, L. K. 2022, *Phys. Rev. D*, 106, 102006, doi: [10.1103/PhysRevD.106.102006](https://doi.org/10.1103/PhysRevD.106.102006)
- Del Pozzo, W., & Nagar, A. 2017, *Phys. Rev. D*, 95, 124034, doi: [10.1103/PhysRevD.95.124034](https://doi.org/10.1103/PhysRevD.95.124034)
- Ewing, B., Huxford, R., Singh, D., et al. 2024, *Phys. Rev. D*, 109, 042008, doi: [10.1103/PhysRevD.109.042008](https://doi.org/10.1103/PhysRevD.109.042008)
- Ezquiaga, J. M., Holz, D. E., Hu, W., Lagos, M., & Wald, R. M. 2021, *Phys. Rev. D*, 103, 064047, doi: [10.1103/PhysRevD.103.064047](https://doi.org/10.1103/PhysRevD.103.064047)
- Finch, E., & Moore, C. J. 2021, *Phys. Rev. D*, 103, 084048, doi: [10.1103/PhysRevD.103.084048](https://doi.org/10.1103/PhysRevD.103.084048)
- Finn, L. S., & Chernoff, D. F. 1993, *Phys. Rev. D*, 47, 2198, doi: [10.1103/PhysRevD.47.2198](https://doi.org/10.1103/PhysRevD.47.2198)
- Gennari, V., Carullo, G., & Del Pozzo, W. 2024, *Eur. Phys. J. C*, 84, 233, doi: [10.1140/epjc/s10052-024-12550-x](https://doi.org/10.1140/epjc/s10052-024-12550-x)
- Ghosh, A., Brito, R., & Buonanno, A. 2021, *Phys. Rev. D*, 103, 124041, doi: [10.1103/PhysRevD.103.124041](https://doi.org/10.1103/PhysRevD.103.124041)
- Ghosh, A., et al. 2016, *Phys. Rev. D*, 94, 021101, doi: [10.1103/PhysRevD.94.021101](https://doi.org/10.1103/PhysRevD.94.021101)
- Ghosh, A., Johnson-Mcdaniel, N. K., Ghosh, A., et al. 2018, *Class. Quant. Grav.*, 35, 014002, doi: [10.1088/1361-6382/aa972e](https://doi.org/10.1088/1361-6382/aa972e)
- GraceDB developers. 2023, GraceDB. <https://git.ligo.org/computing/gracedb>
- Gravitational Wave Open Science Center. 2025, GW230814.230901 data release, doi: <https://doi.org/10.7935/amj3-kd70>
- Gupta, A., et al. 2024, doi: [10.21468/SciPostPhysCommRep.5](https://doi.org/10.21468/SciPostPhysCommRep.5)
- Hamilton, E., London, L., Thompson, J. E., et al. 2021, *Phys. Rev. D*, 104, 124027, doi: [10.1103/PhysRevD.104.124027](https://doi.org/10.1103/PhysRevD.104.124027)
- Hanna, C., et al. 2020, *Phys. Rev. D*, 101, 022003, doi: [10.1103/PhysRevD.101.022003](https://doi.org/10.1103/PhysRevD.101.022003)
- Harry, I., Calderón Bustillo, J., & Nitz, A. 2018, *Phys. Rev. D*, 97, 023004, doi: [10.1103/PhysRevD.97.023004](https://doi.org/10.1103/PhysRevD.97.023004)
- Hofmann, F., Barausse, E., & Rezzolla, L. 2016, *Astrophys. J. Lett.*, 825, L19, doi: [10.3847/2041-8205/825/2/L19](https://doi.org/10.3847/2041-8205/825/2/L19)
- Hoy, C., & Raymond, V. 2021, *SoftwareX*, 15, 100765, doi: <https://doi.org/10.1016/j.softx.2021.100765>
- Hughes, S. A., & Menou, K. 2005, *Astrophys. J.*, 623, 689, doi: [10.1086/428826](https://doi.org/10.1086/428826)
- Isi, M., & Farr, W. M. 2021. <https://arxiv.org/abs/2107.05609>
- Janquart, J., Hannuksela, O. A., K., H., & Van Den Broeck, C. 2021a, *Mon. Not. Roy. Astron. Soc.*, 506, 5430, doi: [10.1093/mnras/stab1991](https://doi.org/10.1093/mnras/stab1991)
- Janquart, J., Seo, E., Hannuksela, O. A., Li, T. G. F., & Broeck, C. V. D. 2021b, *Astrophys. J. Lett.*, 923, L1, doi: [10.3847/2041-8213/ac3bcf](https://doi.org/10.3847/2041-8213/ac3bcf)
- Jiménez-Forteza, X., Keitel, D., Husa, S., et al. 2017, *Phys. Rev. D*, 95, 064024, doi: [10.1103/PhysRevD.95.064024](https://doi.org/10.1103/PhysRevD.95.064024)
- Kamaretsos, I., Hannam, M., Husa, S., & Sathyaprakash, B. S. 2012, *Phys. Rev. D*, 85, 024018, doi: [10.1103/PhysRevD.85.024018](https://doi.org/10.1103/PhysRevD.85.024018)
- Khalil, M., Buonanno, A., Estelles, H., et al. 2023, *Phys. Rev. D*, 108, 124036, doi: [10.1103/PhysRevD.108.124036](https://doi.org/10.1103/PhysRevD.108.124036)
- Kidder, L., et al. 2025, Spectral Einstein Code (SpEC), <https://www.black-holes.org/SpEC.html>
- Klimenko, S., et al. 2016, *Phys. Rev. D*, 93, 042004, doi: [10.1103/PhysRevD.93.042004](https://doi.org/10.1103/PhysRevD.93.042004)
- Koposov, S., Speagle, J., Barbary, K., et al. 2024, joshspeagle/dynesty: v2.1.4, v2.1.4, Zenodo, doi: [10.5281/zenodo.12537467](https://doi.org/10.5281/zenodo.12537467)
- Kumar, P., & Dent, T. 2024, *Phys. Rev. D*, 110, 043036, doi: [10.1103/PhysRevD.110.043036](https://doi.org/10.1103/PhysRevD.110.043036)
- LIGO Scientific Collaboration, Virgo Collaboration, & KAGRA Collaboration. 2018, LVK Algorithm Library - LALSuite, Free software (GPL), doi: [10.7935/GT1W-FZ16](https://doi.org/10.7935/GT1W-FZ16)
- LIGO Scientific, Virgo, and KAGRA Collaboration. 2025, GW230814: investigation of a loud gravitational-wave signal observed with a single detector — Data Release, LIGO-DCC, doi: TBD
- Lindblom, L., Owen, B. J., & Brown, D. A. 2008, *Phys. Rev. D*, 78, 124020, doi: [10.1103/PhysRevD.78.124020](https://doi.org/10.1103/PhysRevD.78.124020)
- Liu, A., Wong, I. C. F., Leong, S. H. W., et al. 2023, *Mon. Not. Roy. Astron. Soc.*, 525, 4149, doi: [10.1093/mnras/stad1302](https://doi.org/10.1093/mnras/stad1302)
- Lo, R. K. L., Li, T. G. F., & Weinstein, A. J. 2019, *Phys. Rev. D*, 99, 084052, doi: [10.1103/PhysRevD.99.084052](https://doi.org/10.1103/PhysRevD.99.084052)
- Lu, N., Ma, S., Piccinni, O. J., Sun, L., & Finch, E. 2025a. <https://arxiv.org/abs/2505.18560>
- . 2025b. <https://arxiv.org/abs/2505.18560>
- LVK Collaboration. 2023, GRB Coordinates Network, 34429, 1
- Ma, S., Sun, L., & Chen, Y. 2023a, *Phys. Rev. D*, 107, 084010, doi: [10.1103/PhysRevD.107.084010](https://doi.org/10.1103/PhysRevD.107.084010)
- . 2023b, *Phys. Rev. Lett.*, 130, 141401, doi: [10.1103/PhysRevLett.130.141401](https://doi.org/10.1103/PhysRevLett.130.141401)
- Ma, S., Mitman, K., Sun, L., et al. 2022, *Phys. Rev. D*, 106, 084036, doi: [10.1103/PhysRevD.106.084036](https://doi.org/10.1103/PhysRevD.106.084036)
- Macleod, D. M., Areeda, J. S., Coughlin, S. B., Massinger, T. J., & Urban, A. L. 2021, *SoftwareX*, 13, 100657, doi: [10.1016/j.softx.2021.100657](https://doi.org/10.1016/j.softx.2021.100657)
- Maggio, E., Silva, H. O., Buonanno, A., & Ghosh, A. 2023, *Phys. Rev. D*, 108, 024043, doi: [10.1103/PhysRevD.108.024043](https://doi.org/10.1103/PhysRevD.108.024043)
- Mehta, A. K., Buonanno, A., Cotesta, R., et al. 2023, *Phys. Rev. D*, 107, 044020, doi: [10.1103/PhysRevD.107.044020](https://doi.org/10.1103/PhysRevD.107.044020)
- Meidam, J., et al. 2018, *Phys. Rev. D*, 97, 044033, doi: [10.1103/PhysRevD.97.044033](https://doi.org/10.1103/PhysRevD.97.044033)
- Messick, C., et al. 2017, *Phys. Rev. D*, 95, 042001, doi: [10.1103/PhysRevD.95.042001](https://doi.org/10.1103/PhysRevD.95.042001)
- Mihaylov, D. P., Ossokine, S., Buonanno, A., et al. 2025, *SoftwareX*, 30, 102080, doi: [10.1016/j.softx.2025.102080](https://doi.org/10.1016/j.softx.2025.102080)

- Mills, C., & Fairhurst, S. 2021, *Phys. Rev. D*, 103, 024042, doi: [10.1103/PhysRevD.103.024042](https://doi.org/10.1103/PhysRevD.103.024042)
- Mirshekari, S., Yunes, N., & Will, C. M. 2012, *Phys. Rev. D*, 85, 024041, doi: [10.1103/PhysRevD.85.024041](https://doi.org/10.1103/PhysRevD.85.024041)
- Mishra, A., Krishnendu, N. V., & Ganguly, A. 2024, *Phys. Rev. D*, 110, 084009, doi: [10.1103/PhysRevD.110.084009](https://doi.org/10.1103/PhysRevD.110.084009)
- Nagar, A., Pratten, G., Riemenschneider, G., & Gamba, R. 2020a, *Phys. Rev. D*, 101, 024041, doi: [10.1103/PhysRevD.101.024041](https://doi.org/10.1103/PhysRevD.101.024041)
- Nagar, A., Riemenschneider, G., Pratten, G., Rettegno, P., & Messina, F. 2020b, *Phys. Rev. D*, 102, 024077, doi: [10.1103/PhysRevD.102.024077](https://doi.org/10.1103/PhysRevD.102.024077)
- Nitz, A., Harry, I., Brown, D., et al. 2024, gwastro/pycbc: v2.3.3 release of PyCBC, v2.3.3, Zenodo, doi: [10.5281/zenodo.10473621](https://doi.org/10.5281/zenodo.10473621)
- Nitz, A. H., Dent, T., Dal Canton, T., Fairhurst, S., & Brown, D. A. 2017, *Astrophys. J.*, 849, 118, doi: [10.3847/1538-4357/aa8f50](https://doi.org/10.3847/1538-4357/aa8f50)
- Nitz, A. H., Dent, T., Davies, G. S., & Harry, I. 2020, *Astrophys. J.*, 897, 169, doi: [10.3847/1538-4357/ab96c7](https://doi.org/10.3847/1538-4357/ab96c7)
- Nitz, A. H., Kumar, S., Wang, Y.-F., et al. 2023, *Astrophys. J.*, 946, 59, doi: [10.3847/1538-4357/aca591](https://doi.org/10.3847/1538-4357/aca591)
- Pai, A., & Arun, K. G. 2013, *Class. Quant. Grav.*, 30, 025011, doi: [10.1088/0264-9381/30/2/025011](https://doi.org/10.1088/0264-9381/30/2/025011)
- Poisson, E., & Will, C. M. 1995, *Phys. Rev. D*, 52, 848, doi: [10.1103/PhysRevD.52.848](https://doi.org/10.1103/PhysRevD.52.848)
- Pompili, L., Maggio, E., Silva, H. O., & Buonanno, A. 2025, <https://arxiv.org/abs/2504.10130>
- Pompili, L., et al. 2023, *Phys. Rev. D*, 108, 124035, doi: [10.1103/PhysRevD.108.124035](https://doi.org/10.1103/PhysRevD.108.124035)
- Pratten, G., et al. 2021, *Phys. Rev. D*, 103, 104056, doi: [10.1103/PhysRevD.103.104056](https://doi.org/10.1103/PhysRevD.103.104056)
- Pürrer, M., & Haster, C.-J. 2020, *Phys. Rev. Res.*, 2, 023151, doi: [10.1103/PhysRevResearch.2.023151](https://doi.org/10.1103/PhysRevResearch.2.023151)
- Ramos-Buades, A., Buonanno, A., Estellés, H., et al. 2023, *Phys. Rev. D*, 108, 124037, doi: [10.1103/PhysRevD.108.124037](https://doi.org/10.1103/PhysRevD.108.124037)
- Romero-Shaw, I. M., et al. 2020, *Mon. Not. Roy. Astron. Soc.*, 499, 3295, doi: [10.1093/mnras/staa2850](https://doi.org/10.1093/mnras/staa2850)
- Roy, S., Haney, M., Pratten, G., Pang, P. T. H., & Van Den Broeck, C. 2025, <https://arxiv.org/abs/2504.21147>
- Sachdev, S., et al. 2019, <https://arxiv.org/abs/1901.08580>
- Sakon, S., et al. 2024, *Phys. Rev. D*, 109, 044066, doi: [10.1103/PhysRevD.109.044066](https://doi.org/10.1103/PhysRevD.109.044066)
- Saleem, M., Datta, S., Arun, K. G., & Sathyaprakash, B. S. 2022, *Phys. Rev. D*, 105, 084062, doi: [10.1103/PhysRevD.105.084062](https://doi.org/10.1103/PhysRevD.105.084062)
- Santamaria, L., et al. 2010, *Phys. Rev. D*, 82, 064016, doi: [10.1103/PhysRevD.82.064016](https://doi.org/10.1103/PhysRevD.82.064016)
- Scheel, M. A., et al. 2025, <https://arxiv.org/abs/2505.13378>
- Schmidt, P., Ohme, F., & Hannam, M. 2015, *Phys. Rev. D*, 91, 024043, doi: [10.1103/PhysRevD.91.024043](https://doi.org/10.1103/PhysRevD.91.024043)
- Shoom, A. A., Gupta, P. K., Krishnan, B., Nielsen, A. B., & Capano, C. D. 2023, *Gen. Rel. Grav.*, 55, 55, doi: [10.1007/s10714-023-03100-z](https://doi.org/10.1007/s10714-023-03100-z)
- Smith, R. J. E., Ashton, G., Vajpeyi, A., & Talbot, C. 2020, *Mon. Not. Roy. Astron. Soc.*, 498, 4492, doi: [10.1093/mnras/staa2483](https://doi.org/10.1093/mnras/staa2483)
- Soni, S., et al. 2025, *Class. Quant. Grav.*, 42, 085016, doi: [10.1088/1361-6382/adc4b6](https://doi.org/10.1088/1361-6382/adc4b6)
- Stein, L. C. 2019, *J. Open Source Softw.*, 4, 1683, doi: [10.21105/joss.01683](https://doi.org/10.21105/joss.01683)
- SXS. 2025, Spectral Einstein Code (SpEC), <https://www.black-holes.org/for-researchers/spec>
- Talbot, C., et al. 2025, <https://arxiv.org/abs/2508.11091>
- Thompson, J. E., Hamilton, E., London, L., et al. 2024, *Phys. Rev. D*, 109, 063012, doi: [10.1103/PhysRevD.109.063012](https://doi.org/10.1103/PhysRevD.109.063012)
- Toubiana, A., & Gair, J. R. 2024, <https://arxiv.org/abs/2401.06845>
- Toubiana, A., Pompili, L., Buonanno, A., Gair, J. R., & Katz, M. L. 2024, *Phys. Rev. D*, 109, 104019, doi: [10.1103/PhysRevD.109.104019](https://doi.org/10.1103/PhysRevD.109.104019)
- Tsang, K. W., Rollier, M., Ghosh, A., et al. 2018, *Phys. Rev. D*, 98, 024023, doi: [10.1103/PhysRevD.98.024023](https://doi.org/10.1103/PhysRevD.98.024023)
- Tsukada, L., et al. 2023, *Phys. Rev. D*, 108, 043004, doi: [10.1103/PhysRevD.108.043004](https://doi.org/10.1103/PhysRevD.108.043004)
- Uchikata, N., Nakano, H., Narikawa, T., et al. 2019, *Phys. Rev. D*, 100, 062006, doi: [10.1103/PhysRevD.100.062006](https://doi.org/10.1103/PhysRevD.100.062006)
- Usman, S. A., et al. 2016, *Class. Quant. Grav.*, 33, 215004, doi: [10.1088/0264-9381/33/21/215004](https://doi.org/10.1088/0264-9381/33/21/215004)
- van de Meent, M., Buonanno, A., Mihaylov, D. P., et al. 2023, *Phys. Rev. D*, 108, 124038, doi: [10.1103/PhysRevD.108.124038](https://doi.org/10.1103/PhysRevD.108.124038)
- Varma, V., Field, S. E., Scheel, M. A., et al. 2019, *Phys. Rev. Research.*, 1, 033015, doi: [10.1103/PhysRevResearch.1.033015](https://doi.org/10.1103/PhysRevResearch.1.033015)
- Veitch, J., Pozzo, W. D., Lyttle, A., et al. 2025, johnveitch/cpnest: v0.11.8, v0.11.8, Zenodo, doi: [10.5281/zenodo.15504752](https://doi.org/10.5281/zenodo.15504752)
- Vijaykumar, A., Mehta, A. K., & Ganguly, A. 2023, *Phys. Rev. D*, 108, 043036, doi: [10.1103/PhysRevD.108.043036](https://doi.org/10.1103/PhysRevD.108.043036)
- Wadekar, D., Roulet, J., Venumadhav, T., et al. 2023, <https://arxiv.org/abs/2312.06631>
- Wette, K. 2020, *SoftwareX*, 12, 100634, doi: [10.1016/j.softx.2020.100634](https://doi.org/10.1016/j.softx.2020.100634)
- Williams, D., Veitch, J., Chiofalo, M. L., et al. 2023, *J. Open Source Softw.*, 8, 4170, doi: [10.21105/joss.04170](https://doi.org/10.21105/joss.04170)
- Woodford, C. J., Boyle, M., & Pfeiffer, H. P. 2019, *Phys. Rev. D*, 100, 124010, doi: [10.1103/PhysRevD.100.124010](https://doi.org/10.1103/PhysRevD.100.124010)
- Wright, M., & Hendry, M. 2021, doi: [10.3847/1538-4357/ac7ec2](https://doi.org/10.3847/1538-4357/ac7ec2)
- Wright, M., Janquart, J., & Johnson-McDaniel, N. K. 2025, *Astrophys. J.*, 981, 133, doi: [10.3847/1538-4357/ad9d3e](https://doi.org/10.3847/1538-4357/ad9d3e)